

The surface code under generic X -error channels: Statistical mechanics, error thresholds, and errorfield double phenomenology

Jan Behrends¹ and Benjamin Béri^{1,2}

¹*T.C.M. Group, Cavendish Laboratory, University of Cambridge, J.J. Thomson Avenue, Cambridge, CB3 0HE, UK*
²*DAMTP, University of Cambridge, Wilberforce Road, Cambridge, CB3 0WA, UK*

We study the surface code under the most general single-qubit X -error channel, encompassing both coherent and incoherent errors. We develop a statistical mechanics mapping for the decoding problem and represent the partition function as a transfer-matrix, i.e., a $(1+1)D$ hybrid quantum circuit. The relevant circuit evolution, as we show, has an efficient matrix product state approximation, using which we develop an algorithm for large-scale syndrome sampling, thus enabling the simulation of these non-Pauli errors away from the limits captured by previous methods. Using these results, we compute maximum-likelihood thresholds and show that error coherence has negligible influence away from the fully coherent limit. We also study how coherence impacts information-theoretic measures like the coherent information, which we show to require, for accurate threshold estimates, increasingly large codes upon increasing error coherence and to eventually break down in the fully coherent limit. To interpret the dominant effect of incoherent errors in large codes, we develop a phenomenological errorfield double field theory, which indicates the instability of coherent errors' above-threshold quasi-long-range order to the above-threshold disorder characteristic of bit-flip errors and the suppression of coherence in the logical noise channel.

I. INTRODUCTION

Quantum error correction (QEC) aims to protect quantum information by significantly suppressing noise [1–4]. Reducing noise is believed to be necessary to achieve quantum advantage [5–7], i.e., for quantum computers that cannot be simulated classically.

A major source of noise is the coupling between a quantum system and its environment [8]. The resulting decoherence of quantum information can be described by stochastic noise that acts probabilistically [9]. However, decoherence is not the only factor that deteriorates quantum information [10–12]: Generally, noise acts as a completely positive trace-preserving [9] (CPTP) quantum channel, which can be mixtures of stochastic (incoherent) noise and unitary (coherent) rotations of qubits. Coherent noise channels, which may arise, e.g., due to spurious gate rotations, can add up constructively, which makes them potentially challenging for QEC [11–16].

A simple example for a mixture of incoherent and coherent contribution is the error channel $\mathcal{E} = \bigotimes_j \mathcal{E}_j$ with

$$\mathcal{E}_j[\rho] = (1 - p_j)\rho + p_j X_j \rho X_j + i\gamma_j \sqrt{(1 - p)} p [X_j, \rho] \quad (1)$$

on qubit j ; \mathcal{E}_j is CPTP [9] when $\gamma_j^2 \leq 1$. Eq. (1) is the most general single-qubit channel one can build using X_j . When $\gamma_j = 0$, it describes incoherent bit flip errors, and when $\gamma_j = \pm 1$, we get coherent errors, namely $\mathcal{E}_j^{(\text{coh})}[\rho] = U_j \rho U_j^\dagger$ with $U_j = e^{\pm i\vartheta_j X_j}$ and $\vartheta_j = \arcsin \sqrt{p_j}$. The error channel (1) thus interpolates between incoherent and coherent limits, which have qualitatively distinct QEC behavior [11–27].

Assessing the impact of such a channel on quantum codes has practical relevance: The existence of an error threshold guarantees exponential suppression of logical errors with increasing code distance [17]. Furthermore, \mathcal{E} also allows one to assess the role of coherence in

error-corrupted many-body states [25, 26, 28–42]. For example, topological order in mixed states has recently been characterized by information-theoretic diagnostics, including quantum relative entropy [43], coherent information [44, 45], and topological entanglement negativity [46, 47], but the focus has mostly been on fully incoherent channels. For such channels, the maximum-likelihood threshold coincides with a topological phase transition in the mixed state [29, 48, 49] and the coherent information can detect this already for small system sizes [49–51]. For coherent errors, however, measures like the coherent information cannot detect a conventional QEC error threshold, since they detect general unitary recoverability (guaranteed for coherent errors) instead of the Pauli-string recoverability relevant for QEC.

Results also exist for fully coherent errors [11, 12, 15, 16, 21–27], which, in surface codes [52–54], include a surprisingly high error threshold and an unusual above-threshold phase with power-law decaying logical error rate [21–24]. The robustness of these features against a small but nonzero incoherent component is however unknown, as is the nature of the error-corrupted many-body state when coherent and incoherent error components act in tandem, as in channel (1) in the simplest case.

In this work, we study the surface code [52–54] under the error channel (1). We focus on the surface code [Fig. 1(a)] due to its experimental relevance [55–58], and known maximum-likelihood thresholds for incoherent [17, 59] and coherent [22] X errors. We develop a statistical mechanics mapping for the decoding problem that expresses error probabilities as partition functions of classical interacting random-bond Ising models (RBIM). To evaluate the partition function numerically, we express it using a transfer matrix [60], i.e., a $(1+1)D$ many-body quantum circuit, shown in Fig. 1(b). As we show, the entanglement entropy of a $1D$ state evolved by the quantum circuit exhibits an area law, and we

can thus efficiently simulate the evolution numerically using matrix product states (MPS) [61, 62]. We leverage this fact to develop a circuit-based sampling algorithm to sample error syndromes according to their approximate probabilities (with the error being controlled by that of the MPS approximation); this enables the simulation of the non-Pauli channel (1) away from the fully coherent and almost fully incoherent regimes accessible to previous methods [11, 24, 27, 63].

Using our mapping, and sampling algorithm, we then compute maximum-likelihood thresholds, which, as we show, depend only weakly on γ_j when sufficiently far from the coherent limit. Due to their practical relevance, we also compute decoder-dependent error thresholds. In particular, we compute thresholds for the minimum-weight perfect matching (MWPM) decoder [64–66].

To characterize our system in terms of mixed-state topological order [28, 29, 48], we also consider two information-theoretic measures: quantum relative entropy and coherent information. We show that for the surface code graph class that our system exemplifies [21], the coherent information of an ensemble of post-measurement mixed states is always constant for coherent errors and thus cannot detect the error correction threshold. We also show numerically that, close to the coherent limit, both coherent information and quantum relative entropy suffer from finite-size effects and are thus unsuited to determine the threshold. They can, however, detect the threshold for large system sizes, provided the error has nonzero incoherent component.

We show the QEC phase diagram in Fig. 1(c) and (d). The maximum-likelihood threshold separates an error-correcting phase from a phase where QEC fails. The threshold is largely independent of the coherent contribution γ until it is close to the coherent limit $\gamma = 1$ [Fig. 1(d)]. The above-threshold phase that we find away from the coherent limit is similar to the above-threshold phase of incoherent errors, i.e., it is characterized by a logical error rate that increases with system size up to a limiting value [67] (1/2 for X errors), and by an area-law entanglement entropy of $1D$ states evolved by the $(1+1)D$ quantum circuit [23, 68]. The above-threshold phase for coherent errors, on the other hand, is characterized by a power-law decreasing logical error rate [22, 24] and a logarithmically increasing entanglement entropy [23, 24]. From our numerical data we conclude that this above-threshold behavior is however a special property of the coherent limit, unstable to a small incoherent noise component.

To provide a theory for the qualitative features of this phase diagram, we develop a phenomenological description using the errorfield double approach [48] based on surface code anyons e and m . The X -error nature of channel (1) allows us to formulate the theory as a non-unitary compact boson field theory of \mathbb{Z}_2 topological order boundary dynamics, with the error-correcting phase corresponding to a gapped edge condensing e anyons. [By a holographic “symmetry topological field theory”

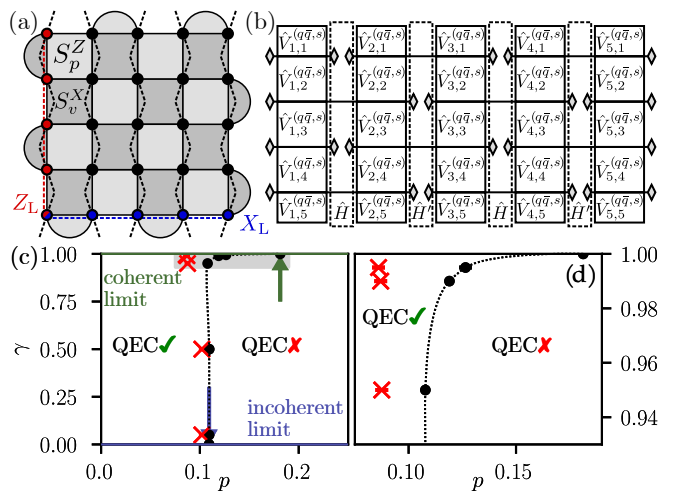


FIG. 1. (a) Surface code ($L = M = 5$) with physical qubits on the vertices (black discs), and alternating S_v^X and S_p^Z stabilizers on the faces of the lattice. The logical X_L and Z_L are denoted by red and blue dashed lines, respectively. We map the surface code to a complex RBIM with two Ising spins σ_v and $\bar{\sigma}_v$ on each S_v^X site. The dashed black lines connect S_v^X sites, constituting vertical slices of the RBIM. (b) Quantum circuit with many-body gates $\hat{V}_{l,m}^{(\gamma\bar{q},s)}$ on physical qubits, where diamonds denote state projection or initialization to $|++\rangle$ (hence adjacent diamonds are projective x -basis measurements with outcome $+1$). The $\hat{V}_{l,m}^{(\gamma\bar{q},s)}$ alternate with layers \hat{H} and \hat{H}' , denoted by dashed rectangles. (c) Approximate phase diagram where the blue and green horizontal lines correspond to the incoherent ($\gamma = 0$) and coherent ($\gamma = 1$) limits. The dotted line denotes the maximum-likelihood threshold separating the error-correcting phase (QEC✓) from a non-correcting phase (QEC✗), where black dots represent numerically calculated values including error bars. Red crosses show the MWPM threshold. Green and blue arrows show the incoherent [17] and coherent [22] maximum-likelihood thresholds, respectively. (d) Part of the phase diagram, indicated in (c) as a gray rectangle.

(SymTFT) [69–79] correspondence, this theory is closely related to our Ising statistical mechanics model, including the error-correcting phase mapping to an ordered phase.] In this theory, a conformal field theory (CFT) emerges from coherent errors above threshold, which is however unstable to perturbations by incoherent noise.

This work is organized as follows: After reviewing, in Sec. II, relevant features of the surface code, in Sec. III we show how information-theoretic measures can be expressed for channel (1). We introduce our statistical-mechanics mapping in Sec. IV and the corresponding $(1+1)D$ quantum circuit in Sec. V. In particular, we discuss symmetry-breaking and entanglement properties of this circuit’s long-time state in Sec. VA and introduce our sampling algorithm in Sec. VB. We compute the error thresholds, giving the phase diagram [Fig. 1(c) and (d)], and information-theoretic quantities in Sec. VI, and develop our phenomenological field theory in Sec. VII. We conclude in Sec. VIII.

II. ERROR CORRECTION IN THE SURFACE CODE

We investigate the surface code under generic single-qubit X errors using the geometry shown in Fig. 1(a). The code consists of mutually commuting stabilizers $S_v^X = \prod_{j \in v} X_j$ and $S_p^Z = \prod_{j \in p} Z_j$, where X_j and Z_j are physical qubit operators on the vertices of a square lattice. The stabilizers form a checkerboard pattern on the faces of the lattice [80, 81]. Bulk stabilizers act on four adjacent qubits, and boundary stabilizers on two qubits. The logical subspace, taken as the +1 eigenspace of all stabilizers, consists of one logical qubit: The logical $X_L = \prod_{j \in \zeta} X_j$, connecting left and right boundaries, and $Z_L = \prod_{j \in \zeta'} Z_j$, connecting top and bottom boundaries, commute with all stabilizers but mutually anticommute, $\{X_L, Z_L\} = 0$. Choosing the operators as in Fig. 1(a), we denote X_L 's path length by L and Z_L 's path length by M . The total number of qubits is $N = LM$.

The QEC recovery procedure consists of two steps: First, all stabilizers are measured, which projects the error-corrupted state $\mathcal{E}[\rho]$ onto the syndrome s . Second, a Pauli string C_s is chosen according to s (typically by a decoder), which returns the state back to the logical subspace. The error channel and subsequent recovery operation act on an initial logical state ρ as

$$D_s[\rho] = \Pi_0 C_s \mathcal{E}[\rho] C_s \Pi_0, \quad (2)$$

with Π_0 the projector onto the logical subspace, and where we have used that the projector onto the syndrome s is $\Pi_s = C_s \Pi_0 C_s$. Due to the projection onto the logical subspace, D_s must be of the form

$$D_s[\rho] = \mathcal{Z}_{00,s} \rho + \mathcal{Z}_{11,s} X_L \rho X_L + \mathcal{Z}_{01,s} \rho X_L + \mathcal{Z}_{10,s} X_L \rho \quad (3)$$

with real coefficients $\mathcal{Z}_{qq,s}$ and generally complex $\mathcal{Z}_{01,s} = \mathcal{Z}_{10,s}^*$. For lattices with only even-weight stabilizers and odd-weight logical operators, as the layout we consider here [Fig. 1(a)], we have $\text{Re} \mathcal{Z}_{01,s} = 0$. Hence, $D_s[\rho]/P(s)$ implements the channel (1) in logical space, where $P(s) = \text{tr}[D_s[\rho]] = \mathcal{Z}_{00,s} + \mathcal{Z}_{11,s}$ is the syndrome probability. The channel in logical space has $p_L^{(s)} = \mathcal{Z}_{11,s}/P(s)$ and $|\gamma_L^{(s)}| = |\mathcal{Z}_{10,s}|/\sqrt{\mathcal{Z}_{00,s}\mathcal{Z}_{11,s}}$.

The syndrome probability $P(s)$ is the sum of the probabilities $P_{0,s} = \mathcal{Z}_{00,s}$ and $P_{1,s} = \mathcal{Z}_{11,s}$ of the error strings C_s and $C_s X_L$ (and equivalent strings), respectively. QEC is possible when the syndrome probability $P(s)$ is on average dominated by one $P_{q,s}$. To assess the feasibility of QEC, we take the infidelity

$$\begin{aligned} r_{q,s} &= 1 - F(\rho_0, \rho_0'^{(q,s)}) = 1 - \frac{\langle 0_L | X_L^q D_s[\rho_0] X_L^q | 0_L \rangle}{P(s)} \\ &= \frac{P_{1-q,s}}{P(s)} \end{aligned} \quad (4)$$

with $\rho_0 = |0_L\rangle\langle 0_L|$ [82] and the post-error and post-correction state $\rho_0'^{(q,s)} = X_L^q D_s[\rho_0] X_L^q$, where $q = 0, 1$ denote the two distinct correction operations C_s and $C_s X_L$.

The logical error rate

$$P_L = \langle \min_q r_{q,s} \rangle_s = \sum_s \min_q P_{q,s} \quad (5)$$

equals the syndrome-averaged minimum infidelity, where $\langle \dots \rangle_s = \sum_s P(s) [\dots]$ denotes the syndrome average.

III. INFORMATION-THEORETIC MEASURES

For incoherent errors, the QEC maximum-likelihood threshold coincides with a phase transition of the error-corrupted mixed state that can be found with information-theoretical diagnostics [28], namely quantum relative entropy, coherent information, and topological entanglement negativity. To elevate these information-theoretic concepts to more generic errors, it is instructive to consider the statistical ensemble of post-error and post-measurement states [83].

Syndrome measurements project the error-corrupted state $\mathcal{E}[\rho_0]$ onto s via $\Pi_s = C_s \Pi_0 C_s$, giving block-diagonal mixed state

$$\rho'_0 = \sum_s \Pi_s \mathcal{E}[\rho_0] \Pi_s = \sum_s C_s D_s[\rho_0] C_s \quad (6)$$

$$= \sum_{sq\bar{q}} \mathcal{Z}_{q\bar{q},s} C_s X_L^q \rho_0 X_L^{\bar{q}} C_s, \quad (7)$$

with the effective channel $D_s[\rho]$ from Eq. (3). Using the complete Hilbert space basis $|\psi_{sq}\rangle = X_L^q C_s |0\rangle$, we obtain the block-diagonal mixed state

$$\rho'_0 = \sum_s (|\psi_{s,0}\rangle, |\psi_{s,1}\rangle) \underbrace{\begin{pmatrix} \mathcal{Z}_{00,s} & \mathcal{Z}_{01,s} \\ \mathcal{Z}_{01,s}^* & \mathcal{Z}_{11,s} \end{pmatrix}}_{=\mathcal{Z}_s} \begin{pmatrix} \langle \psi_{s,0} | \\ \langle \psi_{s,1} | \end{pmatrix} \quad (8)$$

that arises after syndrome measurements, upon discarding the measurement record. The blocks \mathcal{Z}_s are proportional to the density matrices for a given syndrome outcome s . The coherence in \mathcal{Z}_s is also measured by $\gamma_L^{(s)}$.

We shall compare ρ'_0 with $\rho_0'' = X_L \rho_0 X_L$. To this end, we diagonalize \mathcal{Z}_s to obtain a different basis $|\psi'_{s,n}\rangle$ (with $n = 0, 1$), such that $\rho'_0 = \sum_{s,n} \lambda_{s,n} |\psi'_{s,n}\rangle \langle \psi'_{s,n}|$ with eigenvalues

$$\lambda_{s,n} = \frac{1}{2} \left(P(s) - (-1)^n \sqrt{(\mathcal{Z}_{00,s} - \mathcal{Z}_{11,s})^2 + 4|\mathcal{Z}_{01,s}|^2} \right). \quad (9)$$

In the incoherent limit, the $\lambda_{s,n}$ equal the probabilities $P_{q,s}$. In the coherent limit, $\lambda_{s,0} = 0$ and $\lambda_{s,1} = P(s)$.

We now give analytical expressions for the quantum relative entropy and coherent information based on the block-diagonal mixed state, Eq. (6).

A. Quantum relative entropy

The quantum relative entropy between the error-corrupted state ρ'_0 and the state $\rho_0'' = X_L \rho_0 X_L$ takes

the form

$$S_{\text{rel}}(\rho'_0 \parallel \rho''_0) = \text{tr}[\rho'_0 (\ln \rho'_0 - \ln \rho''_0)] \quad (10)$$

$$= \sum_{s,n} (1 - \kappa_s) \lambda_{s,n} \ln \frac{\lambda_{s,n}}{\lambda_{s,1-n}} \quad (11)$$

where we have introduced $\kappa_s = 4(\text{Re}\mathcal{Z}_{01,s})^2 / [(\mathcal{Z}_{00,s} - \mathcal{Z}_{11,s})^2 + 4|\mathcal{Z}_{01,s}|^2]$. Since $\text{Re}\mathcal{Z}_{01,s} = 0$, we have $\kappa_s = 0$.

For incoherent errors, since $\lambda_{s,n} = P_{q=n,s}$, the quantum relative entropy equals the Kullback–Leibler divergence [84] between the probability distributions $P_{q,s}$ and $P_{1-q,s}$,

$$S_{\text{rel}}^{(\text{inc})}(\rho'_0 \parallel \rho''_0) = \sum_{s,q} P_{q,s} \ln \frac{P_{s,1-q}}{P_{s,q}}, \quad (12)$$

which signals the error-correcting threshold [22]—below threshold, $S_{\text{rel}}^{(\text{inc})}$ decreases with code distance exponentially to zero [85].

For coherent errors, the matrix elements are $\mathcal{Z}_{00,s} = |\tilde{\mathcal{Z}}_{0,s}^{(\text{coh})}|^2$, $\mathcal{Z}_{11,s} = |\tilde{\mathcal{Z}}_{1,s}^{(\text{coh})}|^2$, and $\mathcal{Z}_{01,s} = \tilde{\mathcal{Z}}_{0,s}^{(\text{coh})} [\tilde{\mathcal{Z}}_{1,s}^{(\text{coh})}]^*$, where $\tilde{\mathcal{Z}}_{q,s}^{(\text{coh})}$ is a complex single-spin-species RBIM partition function that arises for coherent errors [22], and hence $\lambda_{s,0} = 0$ and $\lambda_{s,1} = P(s)$. In geometries with only even-weight stabilizers and odd-weight logical Pauli operators, coherent errors followed by error correction results in logical subspace rotations, $D_s^{(\text{coh})}[\rho] = e^{iX_L \vartheta_s} \rho e^{-iX_L \vartheta_s}$ [11, 21, 86, 87], which implies

$$S_{\text{rel}}^{(\text{coh})} \Big|_{\text{even}} = \sum_s P_s \ln P_s \quad (13)$$

equals the entropy of the probability distribution, but does not correspond to any QEC threshold indicator.

B. Coherent information

The coherent information is a measure for the recoverability of quantum information [44, 88]. In our setup, we consider a system consisting of three parts: A logical qubit Q , an ancilla R , and an environment E (including stabilizer degrees of freedom) to model the error channel, such that $\text{tr}_{RE}[U_{QE} \rho_{RQE} U_{QE}^\dagger] = \rho'_0$ with ρ'_0 from Eq. (6), where $\rho_Q = \text{tr}_{RE} \rho_{RQE}$ is the density matrix of Q , U_{QE} is a unitary operation acting on Q and E to mimic the error channel, and $\text{tr}_{ER}[\dots]$ denotes the trace over environment E and ancilla R .

Now consider the following procedure to define the coherent information: First prepare Q and R in a Bell-pair superposition, then act unitarily via U_{QE} on the joint system, giving the density matrix $\rho_{RQ'E'}$. Tracing out the environment (and ancilla) yields the coherent information

$$I_C = S[\rho_{Q'}] - S[\rho_{RQ'}], \quad (14)$$

where $S[\rho] = \text{tr}[\rho \ln \rho]$ is the von Neumann entropy of the density matrix ρ , and where $\rho_{Q'} = \text{tr}_{RE'}[\rho_{RQ'E'}]$ and $\rho_{RQ'} = \text{tr}_{E'}[\rho_{RQ'E'}]$.

For the block-diagonal density matrix (6), the coherent information can be expressed as

$$I_C = - \sum_{s,\pm} \left(\frac{P(s)}{2} \pm \text{Re}[\mathcal{Z}_{01,s}] \right) \ln \left(\frac{P(s)}{2} \pm \text{Re}[\mathcal{Z}_{01,s}] \right)$$

$$+ \sum_{s,n} \lambda_{n,s} \ln \lambda_{n,s}, \quad (15)$$

which for even-weight stabilizers and odd-weight logicals simplifies to, again using $\text{Re}[\mathcal{Z}_{01,s}] = 0$,

$$I_C|_{\text{even}} = \sum_s \lambda_{s,q} \ln \frac{2\lambda_{s,q}}{P(s)}. \quad (16)$$

From Eq. (16), we can take the coherent limit, which always gives

$$I_C^{(\text{coh})} \Big|_{\text{even}} = \ln 2, \quad (17)$$

which indicates perfect recoverability. This is not surprising: Since the effective error channel $D_s^{(\text{coh})}[\rho] = e^{iX_L \vartheta_s} \rho e^{-iX_L \vartheta_s}$ acts unitarily on ρ [11], it is—in principle—always possible to correct such rotations. (For even-weight stabilizers and odd-weight logical Pauli operators, this also holds for generic single-qubit coherent errors [86, 87].) However, this does not necessarily imply that the channel is Pauli-string correctable. Considering correctability via Pauli strings yields a threshold at a critical rotation angle [22], which is not captured by the coherent information.

IV. STATISTICAL MECHANICS MAPPING

We now map the coefficients $\mathcal{Z}_{q\bar{q},s}$ to a statistical mechanics model. To this end, we rewrite each local error channel [Eq. (1)] as a sum

$$\mathcal{E}_j[\rho] = \sum_{\substack{x_j=\pm 1 \\ \bar{x}_j=\pm 1}} e^{J_j^{(0)} + J_j^{(1)} x_j + J_j^{(2)} \bar{x}_j + J_j^{(3)} x_j \bar{x}_j} X_j^{\frac{1-x_j}{2}} \rho X_j^{\frac{1-\bar{x}_j}{2}} \quad (18)$$

with couplings (using $\gamma_j > 0$ for simplicity)

$$J_j^{(0)} = \frac{1}{2} \ln [\gamma_j p_j (1 - p_j)], \quad J_j^{(1)} = -\frac{1}{4} \ln \frac{p_j}{1 - p_j} - \frac{i\pi}{4},$$

$$J_j^{(3)} = -\frac{1}{2} \ln \gamma_j \quad J_j^{(2)} = -\frac{1}{4} \ln \frac{p_j}{1 - p_j} + \frac{i\pi}{4}. \quad (19)$$

This enables us to write the total error as a sum over error string configurations

$$\mathcal{E}[\rho] = \sum_{\{x_j, \bar{x}_j\}} e^{\sum_j (J_j^{(0)} + J_j^{(1)} x_j + J_j^{(2)} \bar{x}_j + J_j^{(3)} x_j \bar{x}_j)}$$

$$\times \mathcal{P}(\{x_j\}) \rho \mathcal{P}(\{\bar{x}_j\}) \quad (20)$$

with the Pauli string $\mathcal{P}(\{x_j\}) = \prod_j X_j^{(x_j-1)/2}$. Using the same notation, the error strings $X_L^q C_s = \mathcal{P}(\{\eta_j^{(q,s)}\})$ and $X_L^{\bar{q}} C_s = \mathcal{P}(\{\bar{\eta}_j^{(\bar{q},s)}\})$ with the configuration of signs $\{\eta_j^{(q,s)}\}$ and $\{\bar{\eta}_j^{(\bar{q},s)}\}$. The configurations of $\{\eta_j^{(q,s)}\}$ and $\{\bar{\eta}_j^{(\bar{q},s)}\}$ can only differ on sites with support of X_L .

This implies that the coefficients in $D_s[\rho_0]$ [Eq. (3)] can be expressed as

$$\mathcal{Z}_{q\bar{q},s} = \langle 0 | X_L^q D_s[\rho_0] X_L^{\bar{q}} | 0 \rangle \quad (21)$$

$$= \sum_{\{x_j, \bar{x}_j\}} e^{\sum_j (J_j^{(0)} + J_j^{(1)} x_j + J_j^{(2)} \bar{x}_j + J_j^{(3)} x_j \bar{x}_j)} \quad (22)$$

$$\times \langle 0 | \mathcal{P}(\{\eta_j^{(q,s)}\}) \mathcal{P}(\{x_j\}) | 0 \rangle \langle 0 | \mathcal{P}(\{\bar{x}_j\}) \mathcal{P}(\{\bar{\eta}_j^{(\bar{q},s)}\}) | 0 \rangle,$$

where the matrix overlap is nonzero only when both Pauli strings $\mathcal{P}(\{\eta_j\})\mathcal{P}(\{x_j\})$ and $\mathcal{P}(\{\bar{\eta}_j\})\mathcal{P}(\{\bar{x}_j\})$ form closed loops of X_j operators, i.e., when $\mathcal{P}(\{\eta_j\})\mathcal{P}(\{x_j\}) = \prod_v (S_v^X)^{n_v}$ and $\mathcal{P}(\{\bar{\eta}_j\})\mathcal{P}(\{\bar{x}_j\}) = \prod_v (S_v^X)^{\bar{n}_v}$, respectively. Importantly, the configurations $\{n_v\}$ and $\{\bar{n}_v\}$ do not need to be the same. We describe the implications for x_j (\bar{x}_j is analog): Each sign x_j equals η_j unless exactly one neighboring stabilizer S_v^X is part of the closed-loop configuration. This restricts the sum over configurations of x_j to fewer terms, namely to configurations $\{n_v\}$ of closed loops. Introducing classical Ising spins $\sigma_v = (-1)^{n_v}$, we write $x_{vv'} = \eta_{vv'}^{(q,s)} \sigma_v \sigma_{v'}$, where v label the positions of the S_v^X stabilizers and vv' the bond neighboring v and v' . Writing the sum over configurations of closed loops as a sum over Ising spins, the coefficients have the form of a partition function

$$\mathcal{Z}_{q\bar{q},s} = \sum_{\{\sigma_v, \bar{\sigma}_v\}} \exp[H_{s,q\bar{q}}(\{\sigma_v, \bar{\sigma}_v\})] \quad (23)$$

with

$$H_{s,q\bar{q}} = \sum_{\langle v, v' \rangle} \left(J_{vv'}^{(0)} + J_{vv'}^{(1)} \eta_{vv'}^{(q,s)} \sigma_v \sigma_{v'} + J_{vv'}^{(2)} \bar{\eta}_{vv'}^{(\bar{q},s)} \bar{\sigma}_v \bar{\sigma}_{v'} \right. \\ \left. + J_{vv'}^{(3)} \eta_{vv'}^{(q,s)} \bar{\eta}_{vv'}^{(\bar{q},s)} \sigma_v \sigma_{v'} \bar{\sigma}_v \bar{\sigma}_{v'} \right), \quad (24)$$

where we labeled all couplings $J^{(\mu)}$ ($\mu = \{0, 1, 2, 3\}$) by their neighboring v , and where $\langle v, v' \rangle$ denotes the sum over nearest neighbors. $\mathcal{Z}_{q\bar{q},s}$ is the partition function of a random-bond Ising model with two interacting spin species.

We recover previous results for both coherent and incoherent errors: For coherent errors ($\gamma_j = 1$), the interaction term $J_{vv'}^{(3)} = 0$, which implies that the Ising spins σ_v and $\bar{\sigma}_v$ are decoupled. The partition function thus factorizes into independent sums for each spin species whose couplings $J_{vv'}^{(1)} = (J_{vv'}^{(2)})^*$ are related via complex conjugation, i.e., $\mathcal{Z}_{q\bar{q},s}^{(\text{coh})} = \tilde{\mathcal{Z}}_{q,s}^{(\text{coh})} [\tilde{\mathcal{Z}}_{\bar{q},s}^{(\text{coh})}]^*$, recovering the result for coherent errors [22].

For incoherent errors, the off-diagonal $\mathcal{Z}_{01,s}^{(\text{inc})} = 0$, so we take $q = \bar{q}$. The classical effective Hamiltonian (24)

contains terms $\propto \ln \gamma_{vv'} (1 - \sigma_v \sigma_{v'} \bar{\sigma}_v \bar{\sigma}_{v'})$, which implies that spin configurations with $\sigma_v \sigma_{v'} \bar{\sigma}_v \bar{\sigma}_{v'} = -1$ come with an infinite energy cost when $\gamma_{vv'} \rightarrow 0$. We can thus take $\sigma_v = \bar{\sigma}_v$, which recovers the one-spin-species RBIM for incoherent errors [17].

V. QUANTUM CIRCUIT

To evaluate the partition function [Eq. (23)], we cannot resort to standard methods like Monte-Carlo sampling due to the complex coefficients in the Hamiltonian (24). Instead, we express the partition function as $\mathcal{Z}_{q\bar{q},s} = \langle \phi_0 | \hat{\mathcal{M}}_{q\bar{q},s} | \phi_0 \rangle$ with the transfer matrix

$$\hat{\mathcal{M}}_{q\bar{q},s} = \hat{V}_L^{(q\bar{q},s)} \hat{H}' \hat{V}_{L-1}^{(q\bar{q},s)} \dots \hat{H} \hat{V}_1^{(q\bar{q},s)}, \quad (25)$$

where $\hat{V}_l^{(q\bar{q},s)} = \prod_m \hat{V}_{l,m}^{(q\bar{q},s)}$ denote vertical slices of the transfer matrix, with each $\hat{V}_{l,m}^{(q\bar{q},s)}$ corresponding to one physical qubit at site $j \rightarrow (l, m)$. Because of the geometry of the lattice, we need to include intermediate layers $\hat{H} = \prod_{m=1}^{(M-1)/2} (1 + \tau_{2m}^x)(1 + \bar{\tau}_{2m}^x)$ and $\hat{H}' = \prod_{m=1}^{(M-1)/2} (1 + \tau_{2m-1}^x)(1 + \bar{\tau}_{2m-1}^x)$ between neighboring $\hat{V}_l^{(q\bar{q},s)}$ and $\hat{V}_{l+1}^{(q\bar{q},s)}$ slices, where the Pauli τ_m^μ and $\bar{\tau}_m^\mu$ ($\mu \in \{0, x, y, z\}$) act on $(M-1)$ -site transfer matrix states $|\{\sigma_m \bar{\sigma}_m\}\rangle$, i.e., in a 4^{M-1} -dimensional Hilbert space. When identifying all physical qubits as vertical bonds of a $2D$ lattice that connect S_v^X stabilizer, as denoted in Fig. 1(a) by dashed lines, stabilizers on neighboring slices of this new $2D$ lattice are either identical or uncoupled, as shown in Fig. 1(b). In transfer matrix space, identical spins are horizontally connected via the identity matrix (which gives $\delta_{\sigma\sigma'}$), while uncoupled spins are projected, by $(1 + \tau_m^x)(1 + \bar{\tau}_m^x)$, onto $2|++\rangle$, which by $\sqrt{2}|+\rangle = |0\rangle + |1\rangle$ sums over their configurations.

Apart from boundary terms, the transfer matrices on bonds (l, m) equal

$$\hat{V}_{l,m}^{(q\bar{q},s)} = e^{J_{l,m}^{(0)} + J_{l,m}^{(1)} \eta_{l,m}^{(q,s)} \tau_m^z \tau_{m+1}^z + J_{l,m}^{(2)} \bar{\eta}_{l,m}^{(\bar{q},s)} \bar{\tau}_m^z \bar{\tau}_{m+1}^z} \\ \times e^{J_{l,m}^{(3)} \eta_{l,m}^{(q,s)} \bar{\eta}_{l,m}^{(\bar{q},s)} \tau_m^z \tau_{m+1}^z \bar{\tau}_m^z \bar{\tau}_{m+1}^z} \quad (26)$$

and the boundary state is a product state

$$|\phi_0\rangle = 2^{M-1} \bigotimes_{m=1}^{M-1} |++\rangle_m. \quad (27)$$

We discuss the transfer matrix construction for a different square lattice geometry in the Appendix A.

A. Spontaneous symmetry breaking and entanglement in transfer matrix space

The phases of QEC mirror distinct phases of the quantum circuit [23, 24, 27]. To explore the phases of the quantum circuit in more detail, we use it to define an

effective Hamiltonian $\hat{\mathcal{H}}_{q,s}$ via the thermal density matrix $\hat{\mathcal{M}}_{qq,s}\hat{\mathcal{M}}_{qq,s}^\dagger = \exp(-L\hat{\mathcal{H}}_{q,s})$ with inverse temperature L [22]. Since standard measures for QEC, e.g., the logical error rate defined via the minimum infidelity in Eq. (5), depend only on the diagonal elements $\mathcal{M}_{qq,s}$, with identical bond configurations $\{\eta_{l,m}^{(q,s)}\}$ and $\{\bar{\eta}_{l,m}^{(q,s)}\}$, we focus on $\hat{\mathcal{M}}_{qq,s}$ for this discussion.

The effective Hamiltonian $\hat{\mathcal{H}}_{q,s}$ has an approximate $\mathbb{Z}_2 \times \mathbb{Z}_2$ symmetry defined by the operators $W = \prod_m \tau_m^x$ and $\bar{W} = \prod_m \bar{\tau}_m^x$: W and \bar{W} commute with the intermediate layers \hat{H} and \hat{H}' and with all bulk $\hat{V}_{l,m}^{(qq,s)}$, but not with the gates $\hat{V}_{l,1}^{(qq,s)}$ and $\hat{V}_{l,M}^{(qq,s)}$ at the top and bottom boundaries [in terms of Fig. 1(b)].

Below the QEC threshold, $\hat{\mathcal{H}}_{q,s}$ must be gapped [22–24]. We now relate the gap to the ratio of $P_{0,s} = \mathcal{Z}_{00,s}$ and $P_{1,s} = \mathcal{Z}_{11,s}$: For small $p \rightarrow 0$, the real part of $J_j^{(1)}$ and $J_j^{(2)}$ tend to infinity, hence the effective Hamiltonian is dominated by the $\propto \tau_m^z \bar{\tau}_{m+1}^z$ ($\propto \bar{\tau}_m^z \tau_{m+1}^z$) terms that contribute to $\hat{V}_{l,m}^{(qq,s)}$ [Eq. 26]. The boundary operators $\hat{V}_{l,1}^{(qq,s)}$ and $\hat{V}_{l,M}^{(qq,s)}$ effectively introduce terms $\propto \tau_m^z$ and $\propto \bar{\tau}_m^z$ with $m = 1, M$ to $\hat{\mathcal{H}}_{q,s}$, i.e., they generate a boundary magnetic field [24]. Assuming that both boundary magnetic fields have the same sign for $\hat{\mathcal{H}}_{0,s}$ (the roles of $\mathcal{Z}_{00,s}$ and $\mathcal{Z}_{11,s}$ in the following are reversed when the sign is opposite), the ground state for small p is thus spin-polarized.

Introducing a logical X_L effectively flips one of the boundary magnetic fields by flipping the bonds along X_L , e.g., by flipping the $\eta_{l,M}$ and $\bar{\eta}_{l,M}$ at the bottom for X_L shown in Fig. 1(a). Hence, the lowest-energy states of $\hat{\mathcal{H}}_{1,s}$ must have one domain wall, and there must be approximately M states with similar energies due to the M choices for the position of the domain wall [24]. The energy of such a domain wall state is larger than the energy of the ground state of $\hat{\mathcal{H}}_{0,s}$, roughly by $1/\xi$, where $2/\xi$ is the energy gap of $\hat{\mathcal{H}}_{0,s}$. (Excited states of $\hat{\mathcal{H}}_{0,s}$ have two domain walls.) The ratio of probabilities

$$\frac{P_{1,s}}{P_{0,s}} = \frac{\mathcal{Z}_{11,s}}{\mathcal{Z}_{00,s}} \propto M \exp\left(-\frac{L}{2\xi}\right) \quad (28)$$

thus decreases exponentially to zero, hence, the logical error rate also decreases exponentially to zero.

The behavior of $\hat{\mathcal{H}}_{q,s}$ above threshold is non-universal and depends on the type of error. For incoherent errors, $\hat{\mathcal{H}}_{q,s}$ is gapped but disordered [17, 20, 23]. For coherent errors, $\hat{\mathcal{H}}_{q,s}$ is gapless [22], resulting in critical behavior of the logical error rate [24]. In Sec. VII, we introduce a phenomenological theory, motivated by the anyon description of $\mathcal{Z}_{00,0}$, that captures these properties.

B. Error string sampling

All quantities of interest, e.g., the logical error rate, require a sum over all syndromes. Since the number of possible syndromes scales exponentially with system size, summing over all syndromes becomes unfeasible. In practice we thus take averages $\sum_s P(s)[\dots] = \langle \dots \rangle_s$ over syndromes by sampling s from the probability distribution $P(s)$. For incoherent errors, we can easily sample from $P(s)$ by choosing error strings with $\eta_j = -1$ with probability p_j and $\eta_j = 1$ otherwise. However, for any nonzero coherent contribution γ_j , nontrivial correlations between different j start forming [11, 24]. Hence, we cannot sample directly from $P(s)$. Here we show how to sample distributions $\{\eta\}$ based on the quantum circuit $\hat{\mathcal{M}}$, which was previously described for coherent errors [24]. Since we are interested in probabilities of error strings, we always set $\eta_j = \bar{\eta}_j$ in the following discussion.

The algorithm samples configurations $\{\eta\}$. Each configuration corresponds to an error string that equals, up to stabilizer products, a string $C_s X_s^q$ with some s and q . Thus, the $\{\eta\}$ configurations span all combinations of s and q and we can directly sample configurations $\{\eta\}$ according to their probabilities $P(\{\eta\}) = \mathcal{Z}_{00,s}$. Labeling the many-body gates $\hat{V}_{l,m}^{(qq,s)}$ on vertical links by the site j and sign η_j , $\hat{V}_{l,m}^{(qq,s)} \rightarrow \hat{T}_j^{(\eta_j)}$, the quantum circuit

$$\hat{\mathcal{M}} = \hat{T}_N^{(\eta_N)} \dots \hat{T}_1^{(\eta_1)}, \quad (29)$$

with intermediate gates \hat{H} and \hat{H}' on every M^{th} site. The probability of one error string thus equals

$$P(\{\eta\}) = \langle \phi_0 | \hat{T}_N^{(\eta_N)} \dots \hat{T}_1^{(\eta_1)} | \phi_0 \rangle. \quad (30)$$

Now consider the scenario when all $\eta_{j < N}$ are known and only η_N needs to be determined. Then, we can choose η_N according to its conditional probability $P_N(\eta_N | \eta_{N-1} \dots \eta_1)$, which equals $P(\{\eta\})$ from Eq. (30) divided by the marginal distribution

$$P_{N-1}(\eta_{N-1} \dots \eta_1) = \sum_{\eta_N} \langle \phi_0 | \hat{T}_N^{(\eta_N)} | \phi_{N-1}^{\{\eta\}} \rangle = \langle \omega_N | \phi_{N-1}^{\{\eta\}} \rangle \quad (31)$$

which is found by summing over the two options $\eta_N = \pm 1$, where $\phi_{N-1}^{\{\eta\}} = \hat{T}_{N-1}^{(\eta_{N-1})} \dots \hat{T}_1^{(\eta_1)} | \phi_0 \rangle$ is the initial state evolved by the first $N-1$ qubit gates and intermediate gates \hat{H} and \hat{H}' . The sum over both $\eta_N = \pm 1$ defines the state $|\omega_N\rangle = \sum_{\eta_N} [\hat{T}_N^{(\eta_N)}]^\dagger | \phi_0 \rangle$. The conditional probability $P_{N-1}(\eta_{N-1} | \eta_{N-2} \dots \eta_1)$ equals the marginal probability of the first $N-1$ qubits [Eq. (31)] divided by the marginal probability of the first $N-2$ qubit gates; generally $P_j(\eta_j | \eta_{j-1} \dots \eta_1) = P_j(\eta_j \dots \eta_1) / P_{j-1}(\eta_{j-1} \dots \eta_1)$ for all j .

The expression for the j^{th} marginal probability contains the state (when $j > N-M$)

$$|\omega_{j+1}\rangle = \sum_{\eta_{j+1} \dots \eta_N} [\hat{T}_{j+1}^{(\eta_{j+1})}]^\dagger \dots [\hat{T}_N^{(\eta_N)}]^\dagger | \phi_0 \rangle. \quad (32)$$

We now express $|\omega_j\rangle$ analytically. Starting with $|\phi_0\rangle$ from Eq. (27), we first compute $|\omega_N\rangle$. Choosing $\hat{T}_N^{(\eta_N)}$ such that it acts on the qubit at coordinates L, M , taking the sum of both $\hat{T}_N^{(\pm 1)}$ effectively changes the $(M-1)$ th site in the transfer matrix state from $2|++\rangle_{M-1}$ to $(|00\rangle + |11\rangle)_{M-1}$, which implies

$$|\omega_N\rangle = 2^{M-2} |++\rangle_1 \otimes |++\rangle_2 \dots (|00\rangle + |11\rangle)_{M-1}. \quad (33)$$

Next, $\hat{T}_{N-1}^{(\eta_{N-1})}$ at $(L, M-1)$ effectively changes $2|++\rangle_{M-2} \rightarrow (|00\rangle + |11\rangle)_{M-2}$. This pattern continues until

$$|\omega_{N-M+2}\rangle = \bigotimes_{m=1}^{M-1} (|00\rangle + |11\rangle)_m. \quad (34)$$

To continue to the next site $j = N - M$, we (after summing over the gates $\hat{T}_{N-M+1}^{(\eta_{N-M+1})}$ that do not change $|\omega_{N-M+2}\rangle$) need to apply the layer \hat{H}' ; cf. Fig 1(b). The layer \hat{H}' effectively resets half of the gates to $++$, such that

$$|\omega_{N-M+1}\rangle = 2^{\frac{M-1}{2}} \bigotimes_{m=1}^{\frac{M-1}{2}} (|00\rangle + |11\rangle)_{2m-1} \otimes |++\rangle_{2m}, \quad (35)$$

where even sites are subsequently again changed $2|++\rangle_{2m} \rightarrow (|00\rangle + |11\rangle)_{2m}$ when $T_j^{(\eta_j)}$ acts on them. Similarly, the layer \hat{H} effectively resets the other half of the gates to $++$, such that

$$|\omega_{N-2M+1}\rangle = 2^{\frac{M-1}{2}} \bigotimes_{m=1}^{\frac{M-1}{2}} |++\rangle_{2m-1} \otimes (|00\rangle + |11\rangle)_{2m}. \quad (36)$$

Thanks to its area-law entanglement entropy away from the threshold, we can efficiently represent the evolved state $|\phi_j^{\{\eta\}}\rangle$ as a matrix-product state [61, 62]. Using the truncated MPS and the product-state $|\omega_{j+1}\rangle$, we loop through the system and each site j compute the marginal probabilities $P_j(\eta_j \dots \eta_1) = \langle \omega_{j+1} | \phi_j^{\{\eta\}} \rangle$, and sample η_j using a suitable coin toss.

VI. NUMERICAL THRESHOLD ESTIMATES

We now map out the phase diagram [Fig. 1(c) and (d)] and compute error thresholds. To this end, we numerically simulate the quantum circuit described in Sec. V using MPS [61, 62]. We compute averages over syndromes by drawing syndromes s from the distribution $P(s)$ using the algorithm from Sec. VB, which enables us to compute the logical error rate, quantum relative entropy, and coherent information. We use the syndromes s to additionally compute the minimum weight perfect matching (MWPM) threshold [89, 90]. For all results, we use the

same uniform $p_j \rightarrow p$ and $\gamma_j \rightarrow \gamma$ and take a square geometry with code distance $d = L = M$.

The phase diagram is based on the data shown in Fig. 2. For five different values γ , we show the logical error rate, the MWPM error rate, quantum relative entropy, and coherent information as a function of p for different code distances d .

Fig. 2(a)–(e) shows the logical error rate P_L as a function of p . For $p < p_{\text{th}}$, i.e., below a maximum-likelihood threshold, P_L decreases exponentially with code distance L , and above p_{th} , it increases with L to $P_L \rightarrow 1/2$. We estimate $p_{\text{th}} = \{0.109(1), 0.109(1), 0.108(2), 0.119(2), 0.127(3)\}$ for $\gamma = \{0.05, 0.5, 0.95, 0.99, 0.995\}$, respectively.

Fig. 2(f)–(j) shows the MWPM error rate as a function of p , which we computed using PyMatching [89, 90]. For each syndrome s sampled according to $P(s)$, PyMatching chooses a correction operation equivalent for the error string $C_s X^q$ (with $q^{(\text{MWPM})} \in \{0, 1\}$), whose probability is $P^{(\text{MWPM})}(s) = \mathcal{Z}_{q^{(\text{MWPM})}, q^{(\text{MWPM})}, s}$. The MWPM error rate is averaged over the syndromes and given by $P_L^{(\text{MWPM})} = \langle 1 - P^{(\text{MWPM})}(s) / P(s) \rangle_s$. For $p < p_{\text{th}}^{(\text{MWPM})}$, it decreases exponentially to zero with code distance; for $p > p_{\text{th}}^{(\text{MWPM})}$, it increases up to $P_L^{(\text{MWPM})} \rightarrow 1/2$. From the data in Fig. 2(f)–(j), we estimate $p_{\text{th}}^{(\text{MWPM})} = \{0.102(3), 0.102(3), 0.088(3), 0.087(3), 0.086(3)\}$ for $\gamma = \{0.05, 0.5, 0.95, 0.99, 0.995\}$, respectively. Unlike p_{th} , we find that $p_{\text{th}}^{(\text{MWPM})}$ decreases upon increasing γ towards the coherent limit.

Fig. 2 also shows the quantum relative entropy $S_{\text{rel}}(\rho'_0 \parallel \rho''_0)$ [panels (k)–(o)] and coherent information I_C [panels (p)–(t)]. For all simulations we used the layout in Fig. 1(a), hence $\text{Re}[\mathcal{Z}_{01, s}] = 0$. For small $\gamma \lesssim 0.95$, both $S_{\text{rel}}(\rho'_0 \parallel \rho''_0)$ and I_C signal the transition from the QEC regime to a noncorrecting phase well, even for small code distances. Similar behavior for I_C was observed in Ref. 50 for fully incoherent errors. For $\gamma \gtrsim 0.95$ close to the coherent limit, however, both measures become less reliable for small code distance: For p below threshold, I_C decreases for small d with code distance before it increases again [cf. Fig. 3(a)], thus displaying the expected subthreshold increase only for sufficiently large d .

The behavior of I_C can be explained by considering $|\gamma_L^{(s)}| = |\mathcal{Z}_{10, s}| / \sqrt{\mathcal{Z}_{00, s} \mathcal{Z}_{11, s}}$, the measure, from Secs. II and III, of logical channel coherence. As shown in Fig. 3(b), $\langle |\gamma_L^{(s)}| \rangle_s$ decreases exponentially to zero with d , which holds for all $\gamma < 1$ that we considered. The logical noise thus becomes increasingly incoherent with d . Hence, the coherent information of this channel tends towards the incoherent limit, where it becomes able to signal the QEC threshold. In general, the coherent information can thus be used to distinguish the phases of QEC only for sufficiently large code distances, and only if the error channel has some incoherent component.

To visualize the impact of noise coherence, in Fig. 4

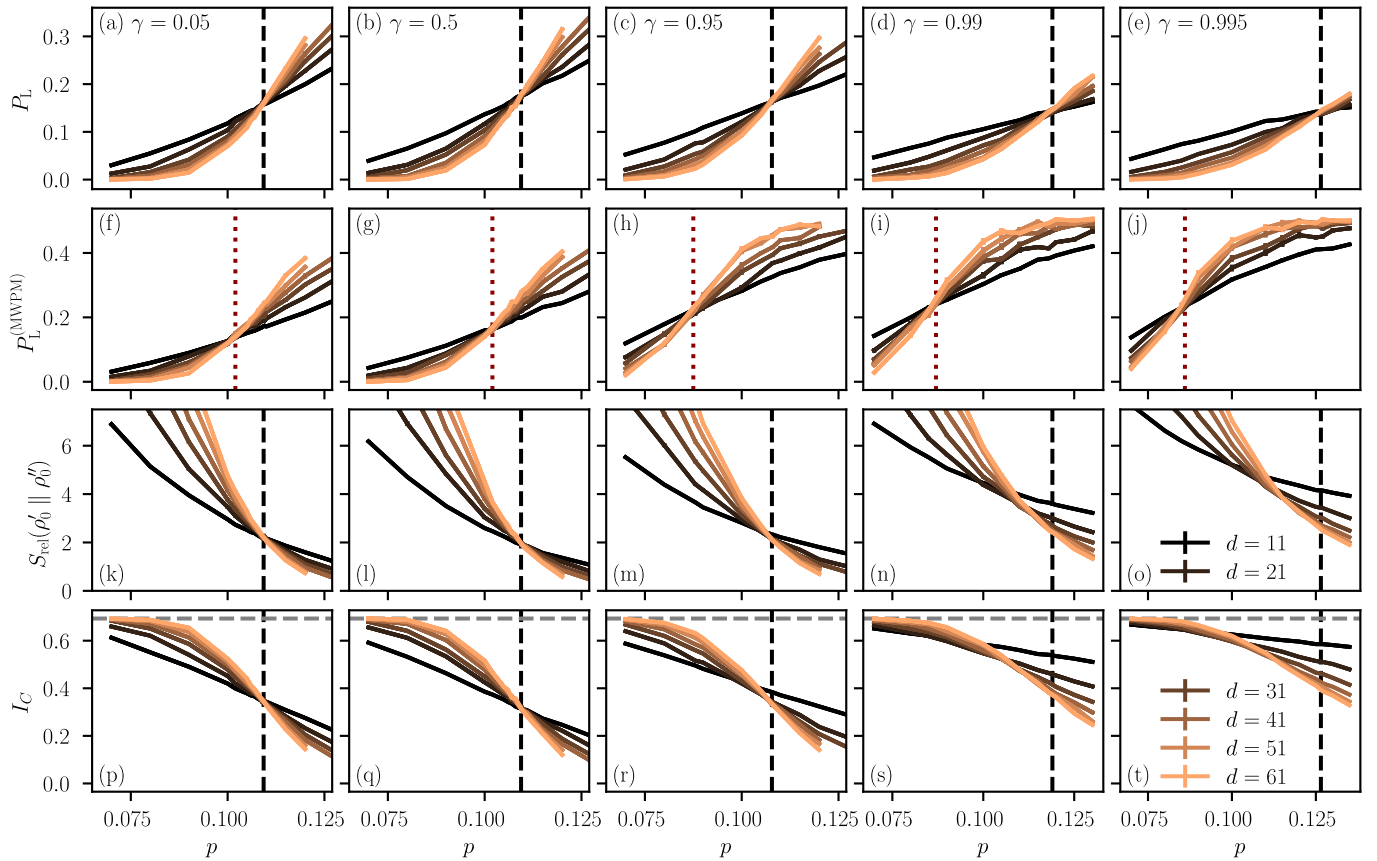


FIG. 2. (a)–(e) Logical error rate, (f)–(j) MWPM error rate, (k)–(o) quantum relative entropy, and (p)–(t) coherent information as a function of p for fixed γ , which increases from left to right. The colors denote different system sizes. Results are averaged over 1000 to 10000 syndromes, and the error bars show the standard error of the mean. The black dashed line shows the approximate maximum likelihood threshold, the red dotted line the MWPM threshold, and the gray dashed line in panels (p)–(t) the perfect-recoverability limit $I_C = \ln 2$ as a guide for the eyes.

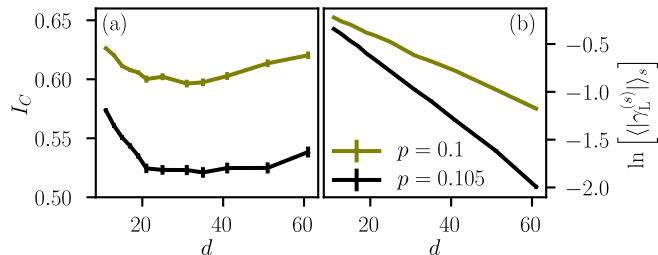


FIG. 3. (a) Coherent information as a function of code distance d for $p = 0.1$, $\gamma = 0.995$ (olive markers) and $p = 0.105$, $\gamma = 0.99$ (black markers). (b) Logical error coherence $\langle |\gamma_L^{(s)}| \rangle_s = \langle |\mathcal{Z}_{10,s}| / \sqrt{\mathcal{Z}_{00,s} \mathcal{Z}_{11,s}} \rangle_s$ as a function of code distance for the same p and γ . (For coherent errors, $|\gamma_L^{(s)}| = 1$.) Data are averaged over 1000 to 10000 syndromes and the error bars show the standard error of the mean.

we show the logical error rate and coherent information as a function of γ for three fixed p : $p = 0.07$ (below p_{th}), $p = 0.12$ (around p_{th}) and $p = 0.2$ (above p_{th}). We plot both quantities as a function of $-\log(1 - \gamma)$ to highlight features visible for large values of γ close to the coherent

limit. The logical error rate starts with a slow increase with γ before reaching a maximum around $\gamma \approx 0.9$, followed by a decrease. At $p = 0.12$, a transition from a non-correcting regime to a QEC regime occurs above $\gamma_{\text{th}} \gtrsim 0.99$. This transition is well-captured by the logical error rate, however, for the system sizes we can simulate numerically, it is not captured by the coherent information, which continues to decrease with system size. At $p = 0.2$ and $\gamma = 0.998$, the behavior of the logical error is inconclusive. More disorder realizations are necessary to resolve the behavior close to the coherent limit. For all p , the coherent information slowly decreases with γ before reaches a minimum around $\gamma \approx 0.9$, and then increases towards $\ln 2$. This is consistent with the observation that the coherent information for even-weight stabilizers and odd-weight logicals always goes to $\log 2$ in the coherent limit, and thus cannot distinguish the quasi-long-range ordered [24] above-threshold behavior from the error-correcting subthreshold regime.

In Fig. 5, we show the half-system entanglement entropy S of the final state $|\phi_N^{\{\eta\}}\rangle$ of the circuit, and its sample standard deviation σ_S as a function of p . Both

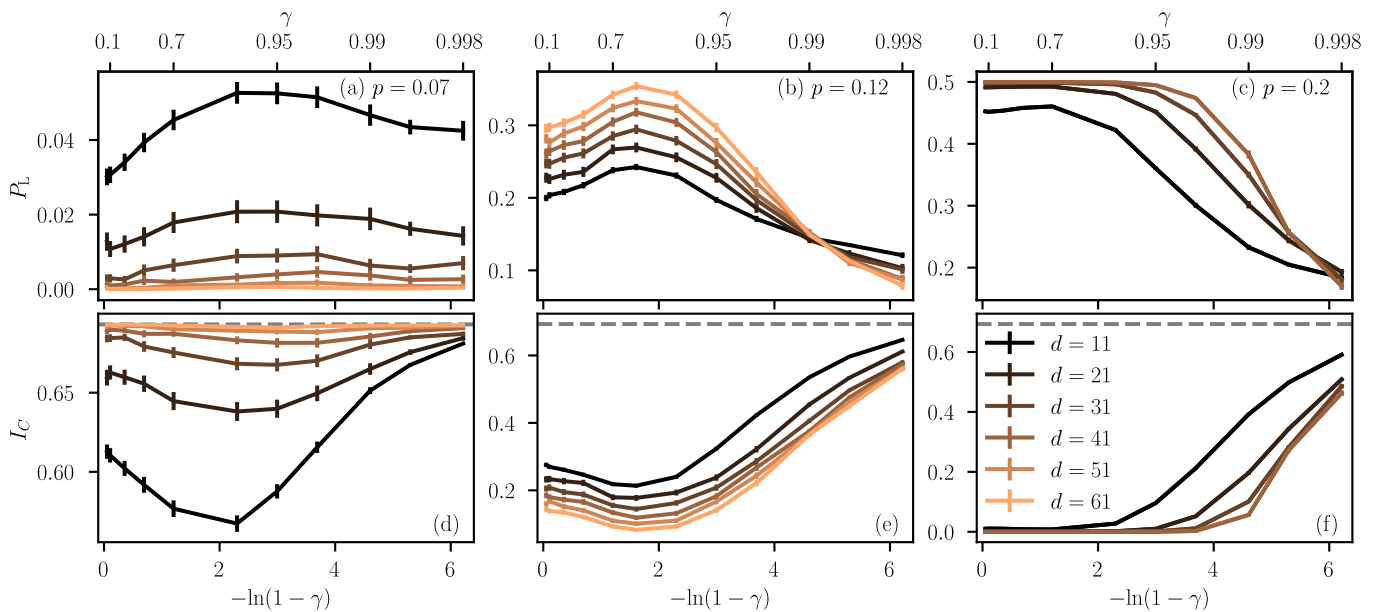


FIG. 4. (a)–(c) Logical error rate and (d)–(f) coherent information as a function of $-\log(1 - \gamma)$ for fixed p , which increases from left to right. Note that we have used an unusual scaling of the x -axis with γ to highlight features visible for large γ close to the coherent limit $\gamma = 1$. (γ itself is shown on the second x axis on top of the panel.) The colors denote different system sizes. Results are averaged over 1000 to 10000 syndromes, and the error bars show the standard error of the mean. The gray dashed line in panels (d)–(f) shows $\ln 2$ as a guide for the eyes.

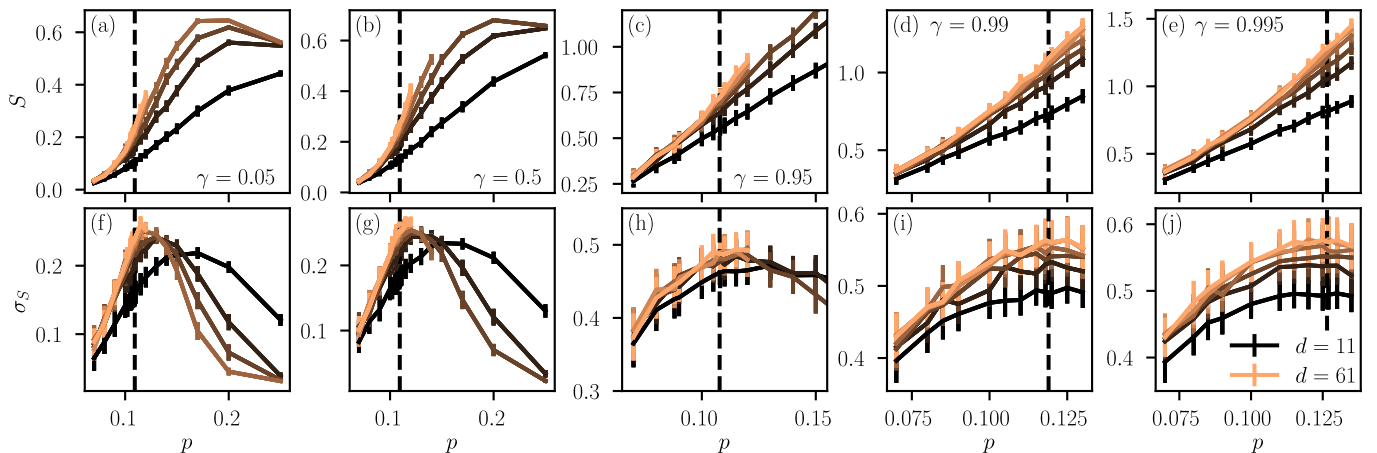


FIG. 5. (a)–(e) Entanglement entropy and (f)–(j) sample standard deviation of half-system entanglement entropy of the quantum circuit. The colors denote different system sizes, and the black dashed line the maximum likelihood threshold. Results are averaged over 1000 to 10000 syndromes, and the error bars show the standard error of the mean.

phases of QEC above and below threshold are characterized by an area law. At the transition, σ_S exhibits a maximum that becomes sharper with increasing system size. Due to the geometry we chose, in particular due to the intermediate transfer matrix layers \hat{H} and \hat{H}' , the entanglement entropy for a bipartition of the final state $|\phi_N^{\{\eta\}}\rangle$ is not a smooth function of the position of the bipartition —since the gates \hat{H} and \hat{H}' in the penultimate layer project half of the sites onto $|++\rangle$ and thereby reduce the entanglement. We suspect the large error bars of σ_S in Fig. 5(h)–(j) are related to the sensitivity of the

entanglement entropy on the position of the bipartition.

One important feature of the resulting phase diagram is the absence of an extended phase with logarithmic entanglement: From our numerics, we cannot find indications of an such a critical regime away from $\gamma = 1$, i.e., fully coherent errors, where such a phase was previously observed [22–24]. Such a critical phase displays logical error rate decaying as a power-law with code distance to a nonzero value [22], and by an approximately logarithmically increasing entanglement entropy [23, 24]. Our numerics thus suggests that this extended critical above-

threshold phase is special to coherent errors.

VII. FIELD THEORY PHENOMENOLOGY

We now discuss a phenomenological model for the structure of the phase diagram in Fig. 1 and the features discussed in the previous section. Our approach is motivated by Ref. 48, but uses a slightly different construction afforded by having only X errors.

We use the fidelity $F(\rho_0, \mathcal{E}[\rho_0]) = \mathcal{Z}_{00,0}$ to motivate our model, however our goal is not to capture the precise behavior of $\mathcal{Z}_{00,0}$, but to deduce structural ingredients using which to describe the phenomenology of the typical $\mathcal{Z}_{q\bar{q},s}$. In particular, the typical $\mathcal{Z}_{00,s}$ will be qualitatively the same as $\mathcal{Z}_{00,0}$ deep in the QEC phase.

Using $|0_L\rangle = 2^{N_v/2} \prod_v \Pi_v |0^{\otimes N}\rangle$, where $\Pi_v = (\mathbb{1} + S_v^X)/2$ and N_v is the number of S_v^X operators,

$$\mathcal{Z}_{00,0} = 2^{N_v} \mathcal{Z}_F, \quad \mathcal{Z}_F = \langle 0^{\otimes N} | \mathcal{E}[\rho_0] | 0^{\otimes N} \rangle. \quad (37)$$

Deep in the error-correcting phase \mathcal{Z}_F is near maximal, while it is suppressed in a non-correcting phase.

Using the mapping $\langle \psi | A \rightarrow A^T | \psi^* \rangle$ for any operator A , we vectorize the density matrix on a space with ket and bra sectors [91–93], and the action of \mathcal{E} becomes

$$\hat{\mathcal{E}} = \prod_j \exp[\kappa_0 + \kappa_1 X_j + \kappa_2 \bar{X}_j + \kappa_3 X_j \bar{X}_j], \quad (38)$$

where X_j and \bar{X}_j act in ket and bra sectors, respectively,

$$\kappa_0 = -\kappa_3 = \frac{1}{4} \log[1 - 4(1 - \gamma^2)p(1 - p)], \quad (39)$$

$$\kappa_1 = -\kappa_2 = \frac{i}{2} \arctan\left(\frac{2\gamma\sqrt{p(1-p)}}{1-2p}\right). \quad (40)$$

Note that $\kappa_3 > 0$ and $\kappa_1 = -\kappa_2$ are imaginary. With vectorization we have

$$\mathcal{Z}_F = \langle\langle 0^{\otimes N} | \hat{\mathcal{E}} | 0_L \rangle\rangle, \quad (41)$$

where $|\psi\rangle\rangle = |\psi\rangle \otimes |\psi^*\rangle$, with $|\psi\rangle \in \{|0_L\rangle, |0^{\otimes N}\rangle\}$, is the product of bra and ket factors.

The state $|0_L\rangle\rangle$ is two copies of the surface code and $\hat{\mathcal{E}}|0_L\rangle\rangle$ is the “errorfield double” [48]. In terms of surface-code anyons e and m , at flipped S_v^X and S_p^Z , respectively, X_j creates a pair of m and \bar{X}_j a pair of \bar{m} in the first and second copy, respectively. The state $|0^{\otimes N}\rangle\rangle$ is invariant under e pair (and \bar{e} pair) creation by Z_j (and \bar{Z}_j) hence condenses e and \bar{e} and confines m and \bar{m} [94–97].

One can view $|0_L\rangle\rangle$ as arising from imaginary time evolution with a surface code Hamiltonian followed by $\hat{\mathcal{E}}$ in the final time-slice, or this time-slice as a spatial boundary by turning a spatial direction into imaginary time [48, 98]. As the nontrivial physics is at this boundary, we get a (1+1) D theory. To qualitatively describe \mathcal{Z}_F , this theory should confine e and \bar{e} in the QEC phase

and see errors competing with this by creating m (and \bar{m}) anyon pairs. Under a holographic SymTFT correspondence [69–79], this boundary physics is a quantum Ising model, matching the Ising nature of our (1+1) D quantum circuits in Sec. V and App. A.

The boundary admits a description as a compact boson field theory [99–102] in terms of slowly varying fields ϕ_e and ϕ_m in the ket sector and $\bar{\phi}_{e,m}$ in the bra sector. As operators, bra and ket fields commute and

$$[\phi_m(x), \phi_e(y)] = i\pi\Theta(x - y), \quad (42)$$

$$[\bar{\phi}_m(x), \bar{\phi}_e(y)] = -i\pi\Theta(x - y), \quad (43)$$

where Θ is the Heaviside function with $\Theta(0) = 1/2$. By the hermiticity of the density matrix, ket and bra sectors form conjugate topological orders [48] and the system has an antiunitary \mathbb{Z}_2^H swap symmetry [92] exchanging $\phi_j \leftrightarrow \bar{\phi}_j$, underlying the sign difference in Eqs. (42) and (43). The field $\psi_e(x) = \exp[\phi_e(x)]$ creates an e and $\psi_m(x) = \exp[i\phi_m(x)]$ an m anyon at position x ; the creation of \bar{e} and \bar{m} works similarly via the $\bar{\phi}_j$ fields.

A. Coherent error limit

We start with fully coherent errors where ϕ_j and $\bar{\phi}_j$ decouple; we focus on the ϕ_j sector. As local processes can create e and m anyons each in pairs, a generic boundary Hamiltonian $H = \int dx h(x)$ has structure [99–102]

$$h = \frac{1}{2\pi} \sum_{\alpha,\beta \in \{e,m\}} V_{\alpha\beta} (\partial_x \phi_\alpha) (\partial_x \phi_\beta) + \sum_{n_e, n_m \in \mathbb{Z}} C_{n_e, n_m} \psi_e^{2n_e} \psi_m^{2n_m}, \quad (44)$$

with real positive definite $V_{\alpha\beta}$ in the kinetic energy term. By $\kappa_{1,2}$ being imaginary, we allow non-Hermitian C_{n_e, n_m} terms, hence we omit the Hermitian conjugate. We next constrain h through the structure and symmetries of $\hat{\mathcal{E}}$ and the requirement of an e -condensing QEC phase.

To implement e condensation, the C_{n_e, n_m} terms include $\cos[2(k_e x + \phi_e)]$ with a real coefficient Δ and momentum k_e . To ensure this survives the integration in $H = \int dx h$ we take $2k_e a = 0 \pmod{2\pi}$, with a the lattice spacing). The e phase operator ϕ_e taking a definite value in the condensate suggests e current $\sim \partial_x \phi_e$ and the ($k = 0$ part of the) e density to be $\sim \partial_x \phi_m$. This suggests $(\partial_x \phi_e)(x) \rightarrow -(\partial_x \phi_e)(-x)$ and $(\partial_x \phi_m)(x) \rightarrow (\partial_x \phi_m)(-x)$ under spatial reflections; this can also be motivated by bosonizing (the Jordan-Wigner transform of) an Ising chain (with $\varphi = 2\phi_m$, $\theta = 2\phi_e$ the standard bosonization fields [103]). By reflection symmetry, odd powers of $\partial_x \phi_e$ are absent from h . In particular $V_{em} = 0$.

Of the other C_{n_e, n_m} terms, we focus on two-anyon processes; higher-orders are expected to be less relevant in the renormalization group (RG). This leaves the m

terms to consider. From the κ_1 term, the m -anyons enter through a Hermitian term times the imaginary unit,

$$h_m = i\mu\partial_x\phi_m + i\mu'\cos[2(k_mx + \phi_m)], \quad (45)$$

with the first term from $\psi_m^\dagger\psi_m$ and the second from $\psi_m^{\dagger 2} + \psi_m^2$ and where μ, μ' are real. Symmetries do not constrain k_m and the logarithmic entanglement phase will require the cosine to be inoperative; since generically $\mu' \neq 0$ we set $2k_ma \neq 0 \pmod{2\pi}$. (The Ising bosonization motivation sees h_m arising from the expansion of the e density and gives $2k_ma = \pi$.) We therefore drop the μ' term (but comment on its effect later). Hence

$$h = \frac{v}{2\pi} [g(\partial_x\phi_e)^2 + g^{-1}(\partial_x\phi_m)^2] + \Delta\cos(2\phi_e) + i\mu\partial_x\phi_m, \quad (46)$$

where $vg = V_{ee}$, $v/g = V_{mm}$, with Luttinger parameter g and velocity v . The bra sector has identical Hamiltonian \bar{h} (with fields $\bar{\phi}_j$), except for $\mu \rightarrow -\mu$ from $\kappa_2 = -\kappa_1$ and also by \mathbb{Z}_2^H symmetry.

To make contact with the free fermions of the coherent-error RBIM, we set $g = 1$ and fermionize h to show that evolution with $\exp(-H)$ leads to an area-law in the e -confining phase ($\Delta \gg |\mu|$) and logarithmic entanglement for $|\mu| \gg \Delta$. We reverse the bosonization identities [103] for $\varphi = 2\phi_m$ and $\theta = 2\phi_e$ to introduce left and right moving fermions χ_+, χ_- , respectively. In terms of $\chi_\pm = (\chi_\pm, \chi_\pm^\dagger)$ we have, up to a constant,

$$h = \frac{1}{2} \sum_{p \in \pm} \chi_p^\dagger \mathcal{H}_{\text{BdG}}^{(p)} \chi_p, \quad \mathcal{H}_{\text{BdG}}^{(\pm)} = (\pm iv\partial_x + i\mu)\Sigma_3 \pm \Delta\Sigma_1, \quad (47)$$

where Σ_j are the Pauli matrices in Nambu space and we absorbed the short distance cutoff a in Δ . The spectrum of $\mathcal{H}_{\text{BdG}}^{(\pm)}$ is $\pm\varepsilon(k) = \pm\sqrt{(\pm vk + i\mu)^2 + \Delta^2}$. For small k , this is $\varepsilon(k) \approx \sqrt{\Delta^2 - \mu^2} \pm ivk\mu/\sqrt{\Delta^2 - \mu^2}$, hence $\text{Re}\varepsilon(k)$ is gapped for $\Delta^2 > \mu^2$ but $\text{Re}\varepsilon(k) \propto vk$ for $\mu^2 < \Delta^2$. For $\Delta^2 > \mu^2$, the $\exp(-H)$ evolution leads to a state akin to the ground state of a gapped system, suggesting an area law. For $\mu^2 > \Delta^2$, the system evolves to a state akin to a CFT ground state suggesting logarithmic entanglement. This behavior is confirmed by recognizing χ_\pm as Jordan-Wigner fermions of a quantum Ising chain in an imaginary transverse field; this yields a system similar to Eq. (46) upon bosonization. This Ising chain has the aforementioned spectral and entanglement features [104–106]. [From the μ' term with $k_m = 0$, \mathcal{H}_{BdG} would include $i\mu'(\chi_+^\dagger\chi_- + \text{h.c.})$, replacing $\text{Re}\varepsilon(k) \propto vk$ with a $\sim \sqrt{(vk)^2 - \mu'^2}$ contribution.]

The CFT becomes concrete for $\mu^2 \gg \Delta^2$; here $\mathcal{H}_{\text{BdG}}^{(\pm)}$ is dominated by the Σ_3 term and its eigenvectors approach $(1, 0)^T$ and $(0, 1)^T$ as $|\mu| \rightarrow \infty$. Hence $\exp(-H)$ evolves to the same state as for $\mu = \Delta = 0$, the free-fermion (or in terms of $\phi_{e,m}$ the free boson) CFT ground state. The main difference is that the pairing term $\Delta\chi_+\chi_-$ now does not connect degenerate states for $k = 0$ (as it would in

the Hermitian case, hence opening a gap) but states that differ in energy by $2i\mu$. Hence $\Delta\chi_+\chi_-$ is a “high-energy” process that can enter the long-distance theory only in second order in perturbation theory.

B. Effect of incoherent noise

Armed with the picture for the coherent case, we can now turn to $\kappa_3 \neq 0$. The direct consequence is the appearance of correlated m -pair- \bar{m} -pair processes,

$$\sum_{n_m \in \mathbb{Z}} C_{n_m} \psi_m^{2n_m} \bar{\psi}_m^{2n_m} + C'_{n_m} \psi_m^{2n_m} \bar{\psi}_m^{-2n_m} + \text{h.c.} \quad (48)$$

We require the terms to be Hermitian because κ_3 is real. In terms of ϕ_j and $\bar{\phi}_j$, focusing on $n_m \leq 1$, we get

$$\lambda_0(\partial_x\phi_m)(\partial_x\bar{\phi}_m) + \lambda_1\cos[2(\phi_m + \bar{\phi}_m)] + \lambda_2\cos[2(\phi_m - \bar{\phi}_m)], \quad (49)$$

By the \mathbb{Z}_2^H symmetry, ϕ_m and $\bar{\phi}_m$ in the cosines are attached the same momentum k_m , that in Eq. (45); this cancels in the λ_2 term and we took the Ising value $k_ma = \pi/2$ in the [later RG-irrelevant, Eq. (54)] λ_1 term.

An indirect consequence is that the coupling between bra and ket sectors allows correlated e terms to appear in perturbation theory. To second order in Δ/μ we get

$$\lambda_3\cos[2(\phi_e + \bar{\phi}_e)] + \lambda_4\cos[2(\phi_e - \bar{\phi}_e)], \quad (50)$$

where we allowed for $\lambda_3 \neq \lambda_4$ anticipating the different RG flow of the two couplings.

We now make contact with spinful Luttinger liquid physics and introduce $\varphi_\uparrow = 2\phi_m$, $\theta_\uparrow = 2\phi_e$, $\varphi_\downarrow = 2\bar{\phi}_m$, $\theta_\downarrow = -2\bar{\phi}_e$, with the standard commutation relation

$$[\varphi_\sigma(x), \theta_\sigma(y)] = 4\pi i\Theta(x - y), \quad \sigma \in \{\uparrow, \downarrow\}. \quad (51)$$

Introducing charge and spin fields $A_c = (A_\uparrow + A_\downarrow)/\sqrt{2}$, $A_s = (A_\uparrow - A_\downarrow)/\sqrt{2}$, for $A \in \{\varphi, \theta\}$, the problem decouples, $H = \int dx (h_c + h_s)$ with

$$h_s = \frac{u_s}{8\pi} [g_s(\partial_x\theta_s)^2 + g_s^{-1}(\partial_x\varphi_s)^2] + i\mu\partial_x\varphi_s/\sqrt{2} + \lambda_2\cos(\sqrt{2}\varphi_s) + \lambda_3\cos(\sqrt{2}\theta_s), \quad (52)$$

and

$$h_c = \frac{u_c}{8\pi} [g_c(\partial_x\theta_c)^2 + g_c^{-1}(\partial_x\varphi_c)^2] + \lambda_1\cos(\sqrt{2}\varphi_c) + \lambda_4\cos(\sqrt{2}\theta_c), \quad (53)$$

where, assuming $g = 1$ for $\kappa_3 = 0$, we have $u_c g_c = u_s g_s = v$ with $g_c = (1 + r\lambda_0)^{-1/2}$ and $g_s = (1 - r\lambda_0)^{-1/2}$, with $r > 0$ constant. Eqs. (52) and (53) are reminiscent of the Hubbard model in an imaginary magnetic field μ and both backscattering and pairing terms in each of the charge and spin sectors. Since $\kappa_3 > 0$, the corresponding coupling in $\exp(-H)$ is negative, hence $\lambda_0 < 0$ and $g_c > 1$, $g_s < 1$, giving an attractive Hubbard model.

Under RG, to first order in the couplings, the cosines flow via $d\lambda/d\ell = (2 - \Delta_\lambda)\lambda$ with the scaling parameter ℓ . The scaling dimensions of the cosines are

$$\Delta_{\lambda_1} = 2g_c, \quad \Delta_{\lambda_2} = 2g_s, \quad \Delta_{\lambda_3} = \frac{2}{g_s}, \quad \Delta_{\lambda_4} = \frac{2}{g_c}. \quad (54)$$

Hence, λ_1 and λ_3 are irrelevant, while λ_2 and λ_4 are relevant under RG. As the charge sector has a Hermitian Hamiltonian, this has the standard interpretation of a gap opening in that sector. In the spin sector we must be more careful because of the large μ term. To this end, we inspect terms, first by fermionizing at $g_s = 1$. In terms of spin-sector fermions χ_{s+}, χ_{s-} , the λ_2 term has $\chi_{s-}^\dagger \chi_{s-} - \chi_{s+} \chi_{s+}^\dagger$ umklapp terms, while the λ_3 term has $\chi_{s-} \chi_{s-} - \chi_{s+} \chi_{s+}$ correlated pairing. As the latter connects states differing in energy by $4i\mu$, it is not a low-energy process, consistently with its RG irrelevance. [A high-energy process from $\cos(2\phi_e) \cos(2\bar{\phi}_e)$ behind Eq. (50) is expected since each of the $\cos(2\phi_e)$ and $\cos(2\bar{\phi}_e)$ are sums of high-energy processes with opposite energies.] The λ_2 term connects degenerate states. To substantiate this opening a gap, we set $\lambda_3 = 0$ and refermionize at $g_s = 1/2$ [103, 107]: $\tilde{\varphi} = \sqrt{2}\varphi_s$ and $\tilde{\theta} = \theta_s/\sqrt{2}$ obey Eq. (51), and h_s becomes Eq. (46) with $g = 1$, $v = u_s$, but with an $i\mu'$ term with $i\mu' \rightarrow \lambda_2$. This maps to spinless fermions in an imaginary chemical potential $i\mu$ and backscattering λ_2 , hence the spectrum is $\varepsilon(k) = \sqrt{(vk)^2 + \lambda_2^2} + i\mu$ with gap λ_2 in the real part.

The field theory thus shows that the logarithmic entanglement for purely coherent errors is fragile; it gives way to an area law (from the gapped phase) upon introducing incoherent noise even as perturbation. This is consistent with our numerical observation of the incoherent parts of the error being dominant. This is also suggestive of the phase boundary approaching, as in Fig. 1(d), the incoherent p value upon increasing incoherent noise, but we leave analyzing this in our field theory to future work.

As the field theory also captures, through e (and \bar{e}) condensation, the correct behavior in the QEC phase, it provides a qualitative description of the phase diagram in Fig. 1. This is further supported by the behavior of the correlation functions phenomenologically corresponding to the typical $\mathcal{Z}_{11,s}/\mathcal{Z}_{00,s}$; the insertion of the $q = \bar{q}$ logical operator $X_L \bar{X}_L$ corresponds to a correlation function with $\exp[i(\phi_m(x) \pm \bar{\phi}_m(x))]$ inserting an m - \bar{m} pair at time 0 which is then removed at time L . By creating kinks of energy $\sim \Delta$ in the ϕ_e and $\bar{\phi}_e$ fields, this decays exponentially with L in the QEC phase; by the emergent CFT it decays as a power law in the coherent non-correcting phase, and, by φ_s being locked at a cosine minimum and commuting with θ_c it has a non-decaying part in the incoherent non-correcting phase.

The theory also captures the phenomenology of the typical logical subspace coherence $\gamma_L^{(s)} = (\mathcal{Z}_{10,s}/\mathcal{Z}_{00,s})/\sqrt{\mathcal{Z}_{11,s}/\mathcal{Z}_{00,s}}$ which corresponds to the ratio of two correlation functions: one with a X_L and the square root of one with a $X_L \bar{X}_L$ insertion. In the purely coherent limit, this correlator ratio equals

one due to the decoupling of ket and bra sectors. In the non-correcting phase with incoherent noise, the correlator for $\sqrt{\mathcal{Z}_{11,s}/\mathcal{Z}_{00,s}}$ is non-decaying as noted above, but $\mathcal{Z}_{10,s}/\mathcal{Z}_{00,s}$ corresponds to an $\exp(\pm i\phi_m)$ correlator featuring a kink in the gapping λ_4 term, leading to an exponential decay. In the QEC phase with incoherent noise, the λ_4 term persists (it is compatible with e and \bar{e} condensation) and gives additional energy penalty to a kink only in the ket sector, corresponding to $\mathcal{Z}_{10,s}/\mathcal{Z}_{00,s}$, compared with half of the energy of the correlated kink-pair from φ_s , corresponding to $\sqrt{\mathcal{Z}_{11,s}/\mathcal{Z}_{00,s}}$. Hence also in this phase we get an exponential decay, capturing the phenomenology of the typical $\gamma_L^{(s)}$ shown in Fig. 3(b).

VIII. CONCLUSION AND OUTLOOK

We have developed a statistical mechanics mapping for the surface code under the most general single-qubit X error channel. We expressed error probabilities as partition functions of classical interacting random-bond Ising models (RBIM) with complex couplings. We also showed that the ensemble of error-corrupted states, Eq. (8), that arises after syndrome measurements can be expressed using RBIM partition functions. Using this representation, we computed information-theoretic quantities of the mixed state to characterize its topological order.

We demonstrated that a coherent contribution to an incoherent error channel does not significantly affect the logical error rate or the maximum-likelihood threshold until it is close to the fully coherent limit, cf. Fig. 2. We also found that the coherence $\gamma_L^{(s)}$ of the logical noise decreases with code distance for any nonzero incoherent noise component (Fig. 3). The logical error rate as a function of γ [characterizing the coherent noise component in Eq. (1)] initially slightly increases before it decreases again close to the coherent limit, cf. Fig. 4. This decreasing logical error rate results in an increased maximum-likelihood threshold close to the coherent limit.

We have also developed a phenomenological errorfield double field theory that can account for some of these qualitative features, including the behavior of the logical error rate and the suppression of $\gamma_L^{(s)}$. This field theory gives analytical support to the observed fragility of the quasi-long-range ordered above-threshold behavior for fully coherent errors by showing that the incoherent noise component enters as a relevant perturbation to the critical above-threshold regime of the coherent case.

The statistical-mechanics mapping developed here gives access to the full ensemble of post-measurement states. This facilitates the computation of information-theoretic quantities that are nonlinear in the density matrix, namely the coherent information and quantum relative entropy. We could show that the coherent information of this ensemble subject to fully coherent errors always goes to $\ln 2$ in geometries where stabilizers have even weight and logicals have odd weight; this conclusion

also holds for generic $SU(2)$ single-qubit coherent errors. For generic X errors close to the coherent limit, both coherent information and quantum relative entropy suffer from finite size effects; this can be explained by $\gamma_L^{(s)}$ requiring large codes to become sufficiently suppressed.

A key ingredient for these results is our syndrome sampling algorithm. This is based on evaluating the quantum circuit (i.e., transfer matrix) evolution using matrix-product states, hence it samples syndromes according to their approximate probability. This algorithm can be used with any decoder as we illustrated by computing thresholds for minimum weight perfect matching. This threshold—unlike the maximum-likelihood-threshold—decreases with increasing coherence γ .

Our work forms the basis for statistical-mechanics mappings and transfer matrix calculations of generic single-qubit error channels, as we sketch in the Appendix B. We expect that the large parameter space of such generic channels can be explored using similar techniques to those in this work since we expect the below-threshold regime to be generally characterized by an area-law entanglement entropy, and hence to be efficiently simulable using matrix product states.

Studying the impact of generic single-qubit error channels is not only relevant for a quantum memory, but also for state preparation [87, 108] and teleportation [83], and decoder-encoder problems [109]. We expect that our work can be extended to these interesting areas.

Note added. During the completion of this manuscript, we became aware of a related independent work on sampling and maximum likelihood decoding in the surface code under local noise [110].

ACKNOWLEDGMENTS

We thank Florian Venn for collaboration on related topics, Max McGinley for input on information-theoretic measures, Claudio Castelnovo for providing additional computational resources, and Xhek Turkeshi for helpful discussions. This work was supported by EPSRC Grant No. EP/V062654/1, a Leverhulme Early Career Fellowship and the Newton Trust of the University of Cambridge. Our simulations used resources at the Cambridge Service for Data Driven Discovery operated by the University of Cambridge Research Computing Service (www.csd3.cam.ac.uk), provided by Dell EMC and Intel using EPSRC Tier-2 funding via grant EP/T022159/1, and STFC DiRAC funding (www.dirac.ac.uk).

Appendix A: Quantum circuit in different geometry

In the main text, we chose a geometry with qubits on vertices of lattice, a “rotated” surface code [80, 81]. Here we show for completeness the construction of the quantum circuit for another geometry of surface code with “rough” and “smooth” boundaries [53].

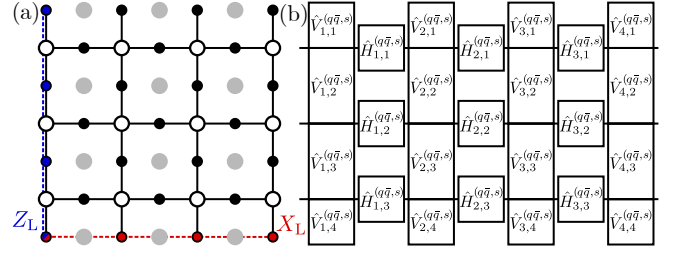


FIG. 6. (a) Surface code ($L = M = 4$) with rough and smooth boundaries on a square lattice, with physical qubits (black discs) on its links, S_v^X stabilizers on its vertices (open discs), and S_p^Z on its faces (gray discs). The logical X_L and Z_L are denoted by red and blue dashed lines, respectively. (b) The quantum circuit consists of $\hat{V}_{l,m}^{(q\bar{q},s)}$ gates on vertical links and $\hat{H}_{l,m}^{(q,s)}$ on horizontal links.

In this geometry, qubits are located on the links of the lattice, and the S_v^X and S_p^Z stabilizers on the vertices and plaquettes of the lattice, respectively; cf. Fig. 6(a). The mapping to a complex RBIM Ising model is analog to the main text, but now Ising spins $\sigma_v, \bar{\sigma}_v$ are located on the vertices of the lattice. To construct the quantum circuit, we distinguish horizontal and vertical couplings between these spins, analogous to the transfer matrix construction for the noninteracting RBIM with spins on vertices of a 2D square lattice [60]; cf. Fig. 6(b).

The $\hat{V}_{l,m}$ matrices on the vertical bonds have the same form as given in Eq. (26). The matrices on the horizontal bonds factorize for the l^{th} layer as $\hat{H}_l = \prod_m \hat{H}_{l,m}$ with the matrices

$$\hat{H}_{l,m}^{(q\bar{q},s)} = \exp \left(\kappa_{l,m}^{(0)} + \kappa_{l,m}^{(1)} \tau_m^x + \kappa_{l,m}^{(2)} \bar{\tau}_m^x + \kappa_{l,m}^{(3)} \tau_m^x \bar{\tau}_m^x \right). \quad (\text{A1})$$

The couplings are given by

$$\begin{aligned} \kappa_{l,m}^{(0)} &= \frac{1}{4} \ln [1 - 4p(1-p)(1-\gamma^2)] + \frac{i\pi}{4} (\eta_{l,m}^{(h)} - \bar{\eta}_{l,m}^{(h)}), \\ \kappa_{l,m}^{(1)} &= \frac{i}{2} \arctan \left(\frac{2\gamma\sqrt{p(1-p)}}{1-2p} \right) + \frac{i\pi}{4} (1 - \eta_{l,m}^{(h)}), \\ \kappa_{l,m}^{(2)} &= -\frac{i}{2} \arctan \left(\frac{2\gamma\sqrt{p(1-p)}}{1-2p} \right) - \frac{i\pi}{4} (1 - \bar{\eta}_{l,m}^{(h)}), \\ \kappa_{l,m}^{(3)} &= -\frac{1}{4} \ln [1 - 4p(1-p)(1-\gamma^2)], \end{aligned} \quad (\text{A2})$$

where we introduced the superscript h to indicate horizontal bonds.

Appendix B: Generic error channel

The construction we introduced in this work can be extended to a more generic local error channel

$$\begin{aligned} \mathcal{E}_j^{(f)}[\rho] &= \sum_{\mu\nu} \varepsilon_{\mu\nu} \mathcal{O}_j^\mu \rho \mathcal{O}_j^\nu \\ &= \sum_{\substack{x_j, \bar{x}_j \\ z_j, \bar{z}_j}} e^{h(\{x_j, z_j, \bar{x}_j, \bar{z}_j\})} X_j^{\frac{1-x_j}{2}} Z_j^{\frac{1-z_j}{2}} \rho Z_j^{\frac{1-\bar{z}_j}{2}} X_j^{\frac{1-\bar{x}_j}{2}} \end{aligned} \quad (\text{B1})$$

involving all on-site Pauli operators $\mathcal{O}_j^\mu = (\mathbb{1}_j, X_j, Y_j, Z_j)$ for $\mu = \{0, 1, 2, 3\}$. In this expansion, we express the 16

parameters [111] $\varepsilon_{\mu\nu}$ as

$$\begin{aligned} h &= J_j^{(0)} + J_j^{(x)} x_j + J_j^{(y)} x_j z_j + J_j^{(z)} z_j + J_j^{(\bar{x})} \bar{x}_j + J_j^{(\bar{y})} \bar{x}_j \bar{z}_j \\ &\quad + J_j^{(\bar{z})} \bar{z}_j + J_j^{(x\bar{x})} x_j \bar{x}_j + J_j^{(y\bar{y})} x_j z_j \bar{x}_j \bar{z}_j + J_j^{(z\bar{z})} z_j \bar{z}_j \\ &\quad + J_j^{(x\bar{y})} x_j \bar{x}_j \bar{z}_j + J_j^{(y\bar{x})} x_j z_j \bar{x}_j + J_j^{(y\bar{z})} x_j z_j \bar{z}_j \\ &\quad + J_j^{(z\bar{y})} z_j \bar{x}_j \bar{z}_j + J_j^{(z\bar{x})} z_j \bar{x}_j + J_j^{(x\bar{z})} x_j \bar{z}_j. \end{aligned} \quad (\text{B2})$$

Analogous to the error channel discussed in the main text, the total error channel $\mathcal{E}^{(f)} = \bigotimes_j \mathcal{E}_j^{(f)}$ projected onto a stabilizer measurement can be expressed using complex coefficients $Z_{\mu\nu, s}^{(f)}$ that equal partition functions of interacting Ising models. The Ising model will host two spin species on both direct and dual lattice. Interaction terms couple both spin species within each lattice, and direct and dual lattice via four-spin, eight-spin, and sixteen-spin interaction terms.

Since the error-correcting phase must be characterized by an area law in the transfer matrix space [22, 23], we expect that efficient simulations using matrix product states are possible. We also expect that the sampling of error strings is possible using a variant of the algorithm discussed in Sec. VB. This algorithm relies on an analytical expression of the state $|\omega_j\rangle$ [Eq. (32)]. If the sum over all four [24] configurations of $[\hat{T}_j^{(\eta_j)}]^\dagger |\omega_{j+1}\rangle$ can be expressed as a product state, the other steps of the algorithm follow through. We leave investigating this possibility to future works.

-
- [1] P. W. Shor, Scheme for reducing decoherence in quantum computer memory, *Physical Review A* **52**, R2493 (1995).
 - [2] A. R. Calderbank and P. W. Shor, Good quantum error-correcting codes exist, *Physical Review A* **54**, 1098 (1996).
 - [3] A. M. Steane, Error Correcting Codes in Quantum Theory, *Physical Review Letters* **77**, 793 (1996).
 - [4] J. Preskill, Quantum Computing in the NISQ era and beyond, *Quantum* **2**, 79 (2018).
 - [5] A. M. Dalzell, N. Hunter-jones, and F. G. S. L. Brandão, Random quantum circuits transform local noise into global white noise, [arXiv:2111.14907](https://arxiv.org/abs/2111.14907).
 - [6] D. Stilck França and R. García-Patrón, Limitations of optimization algorithms on noisy quantum devices, *Nature Physics* **17**, 1221 (2021).
 - [7] D. Hangleiter and J. Eisert, Computational advantage of quantum random sampling, *Reviews of Modern Physics* **95**, 035001 (2023).
 - [8] W. H. Zurek, Decoherence, einselection, and the quantum origins of the classical, *Reviews of Modern Physics* **75**, 715 (2003).
 - [9] M. A. Nielsen and I. L. Chuang, *Quantum Computation and Quantum Information* (Cambridge University Press, Cambridge, U.K., 2010).
 - [10] C. Chamberland, J. Wallman, S. Beale, and R. Laflamme, Hard decoding algorithm for optimizing thresholds under general Markovian noise, *Physical Review A* **95**, 042332 (2017).
 - [11] S. Bravyi, M. Englbrecht, R. König, and N. Peard, Correcting coherent errors with surface codes, *npj Quantum Inf.* **4**, 55 (2018).
 - [12] D. Gottesman, Maximally Sensitive Sets of States, [arXiv:1907.05950](https://arxiv.org/abs/1907.05950).
 - [13] M. Gutiérrez, C. Smith, L. Lulushi, S. Janardan, and K. R. Brown, Errors and pseudothresholds for incoherent and coherent noise, *Physical Review A* **94**, 042338 (2016).
 - [14] E. Huang, A. C. Doherty, and S. Flammia, Performance of quantum error correction with coherent errors, *Physical Review A* **99**, 022313 (2019).
 - [15] D. Greenbaum and Z. Dutton, Modeling coherent errors in quantum error correction, *Quantum Science and Technology* **3**, 015007 (2018).
 - [16] J. K. Iverson and J. Preskill, Coherence in logical quantum channels, *New Journal of Physics* **22**, 073066 (2020).
 - [17] E. Dennis, A. Kitaev, A. Landahl, and J. Preskill, Topological quantum memory, *J. Math. Phys.* **43**, 4452 (2002).
 - [18] H. Bombin, R. S. Andrist, M. Ohzeki, H. G. Katzgraber, and M. A. Martin-Delgado, Strong Resilience of Topological Codes to Depolarization, *Physical Review X* **2**, 021004 (2012).

- [19] J. R. Wootton and D. Loss, High Threshold Error Correction for the Surface Code, *Physical Review Letters* **109**, 160503 (2012).
- [20] C. T. Chubb and S. T. Flammia, Statistical mechanical models for quantum codes with correlated noise, *Annales de l'Institut Henri Poincaré D* **8**, 269 (2021).
- [21] F. Venn and B. Béri, Error-correction and noise-decoherence thresholds for coherent errors in planar-graph surface codes, *Phys. Rev. Res.* **2**, 043412 (2020).
- [22] F. Venn, J. Behrends, and B. Béri, Coherent-Error Threshold for Surface Codes from Majorana Delocalization, *Physical Review Letters* **131**, 060603 (2023).
- [23] J. Behrends, F. Venn, and B. Béri, Surface codes, quantum circuits, and entanglement phases, *Physical Review Research* **6**, 013137 (2024).
- [24] J. Behrends and B. Béri, Statistical mechanical mapping and maximum-likelihood thresholds for the surface code under generic single-qubit coherent errors, [arXiv:2410.22436](https://arxiv.org/abs/2410.22436).
- [25] Y.-H. Chen and T. Grover, Unconventional topological mixed-state transition and critical phase induced by self-dual coherent errors, [arXiv:2403.06553](https://arxiv.org/abs/2403.06553).
- [26] S. Lee and E.-G. Moon, Mixed-State Topological Order under Coherent Noises, [arXiv:2411.03441](https://arxiv.org/abs/2411.03441).
- [27] Y. Bao and S. Anand, Phases of decodability in the surface code with unitary errors, [arXiv:2411.05785](https://arxiv.org/abs/2411.05785).
- [28] R. Fan, Y. Bao, E. Altman, and A. Vishwanath, Diagnostics of mixed-state topological order and breakdown of quantum memory, [arXiv:2301.05689](https://arxiv.org/abs/2301.05689).
- [29] J. Y. Lee, C.-M. Jian, and C. Xu, Quantum Criticality Under Decoherence or Weak Measurement, *PRX Quantum* **4**, 030317 (2023).
- [30] Y.-H. Chen and T. Grover, Separability Transitions in Topological States Induced by Local Decoherence, *Physical Review Letters* **132**, 170602 (2024).
- [31] S. Sang, Y. Zou, and T. H. Hsieh, Mixed-state Quantum Phases: Renormalization and Quantum Error Correction, [arXiv:2310.08639](https://arxiv.org/abs/2310.08639).
- [32] N. Myerson-Jain, T. L. Hughes, and C. Xu, Decoherence through Ancilla Anyon Reservoirs, [arXiv:2312.04638](https://arxiv.org/abs/2312.04638).
- [33] K. Su, Z. Yang, and C.-M. Jian, Tapestry of dualities in decohered quantum error correction codes, [arXiv:2401.17359](https://arxiv.org/abs/2401.17359).
- [34] Z. Li and R. S. K. Mong, Replica topological order in quantum mixed states and quantum error correction, [arXiv:2402.09516](https://arxiv.org/abs/2402.09516).
- [35] A. Lavasani and S. Vijay, The Stability of Gapped Quantum Matter and Error-Correction with Adiabatic Noise, [arXiv:2402.14906](https://arxiv.org/abs/2402.14906).
- [36] A. Lyons, Understanding Stabilizer Codes Under Local Decoherence Through a General Statistical Mechanics Mapping, [arXiv:2403.03955](https://arxiv.org/abs/2403.03955).
- [37] R. Sohal and A. Prem, A Noisy Approach to Intrinsically Mixed-State Topological Order, [arXiv:2403.13879](https://arxiv.org/abs/2403.13879).
- [38] T.-C. Lu, Disentangling transitions in topological order induced by boundary decoherence, [arXiv:2404.06514](https://arxiv.org/abs/2404.06514).
- [39] S. Sang and T. H. Hsieh, Stability of mixed-state quantum phases via finite Markov length, [arXiv:2404.07251](https://arxiv.org/abs/2404.07251).
- [40] T. Ellison and M. Cheng, Towards a classification of mixed-state topological orders in two dimensions, [arXiv:2405.02390](https://arxiv.org/abs/2405.02390).
- [41] Z. Zhang, U. Agrawal, and S. Vijay, Quantum Communication and Mixed-State Order in Decohered Symmetry-Protected Topological States, [arXiv:2405.05965](https://arxiv.org/abs/2405.05965).
- [42] H. Oshima, K. Mochizuki, R. Hamazaki, and Y. Fuji, Topology and Spectrum in Measurement-Induced Phase Transitions, [arXiv:2412.11097](https://arxiv.org/abs/2412.11097).
- [43] H. Umegaki, Conditional expectation in an operator algebra. IV. Entropy and information, *Kodai Mathematical Journal* **14**, 59 (1962).
- [44] B. Schumacher and M. A. Nielsen, Quantum data processing and error correction, *Physical Review A* **54**, 2629 (1996).
- [45] S. Lloyd, Capacity of the noisy quantum channel, *Physical Review A* **55**, 1613 (1997).
- [46] K. Życzkowski, P. Horodecki, A. Sanpera, and M. Lewenstein, Volume of the set of separable states, *Physical Review A* **58**, 883 (1998).
- [47] Y. A. Lee and G. Vidal, Entanglement negativity and topological order, *Physical Review A* **88**, 042318 (2013).
- [48] Y. Bao, R. Fan, A. Vishwanath, and E. Altman, Mixed-state topological order and the errorfield double formulation of decoherence-induced transitions, [arXiv:2301.05687](https://arxiv.org/abs/2301.05687).
- [49] Z.-M. Huang, L. Colmenarez, M. Müller, and S. Diehl, Coherent information as a mixed-state topological order parameter of fermions, [arXiv:2412.12279](https://arxiv.org/abs/2412.12279).
- [50] L. Colmenarez, Z.-M. Huang, S. Diehl, and M. Müller, Accurate optimal quantum error correction thresholds from coherent information, *Physical Review Research* **6**, L042014 (2024).
- [51] L. Colmenarez, S. Kim, and M. Müller, Fundamental thresholds for computational and erasure errors via the coherent information, [arXiv:2412.16727](https://arxiv.org/abs/2412.16727).
- [52] A. Y. Kitaev, Quantum computations: algorithms and error correction, *Russian Mathematical Surveys* **52**, 1191 (1997).
- [53] S. B. Bravyi and A. Y. Kitaev, Quantum codes on a lattice with boundary, [arXiv:quant-ph/9811052](https://arxiv.org/abs/quant-ph/9811052) [[quant-ph](https://arxiv.org/abs/quant-ph/9811052)] (1998).
- [54] M. H. Freedman and D. A. Meyer, Projective plane and planar quantum codes, [arXiv:quant-ph/9810055](https://arxiv.org/abs/quant-ph/9810055) [[quant-ph](https://arxiv.org/abs/quant-ph/9810055)] (1998).
- [55] Google Quantum AI, Suppressing quantum errors by scaling a surface code logical qubit, *Nature* **614**, 676 (2023).
- [56] D. Bluvstein *et al.*, Logical quantum processor based on reconfigurable atom arrays, *Nature* **626**, 58 (2024).
- [57] Google Quantum AI, Quantum error correction below the surface code threshold, *Nature* [10.1038/s41586-024-08449-y](https://doi.org/10.1038/s41586-024-08449-y) (2024).
- [58] Google Quantum AI, Demonstrating dynamic surface codes, [arXiv:2412.14360](https://arxiv.org/abs/2412.14360).
- [59] F. Merz and J. T. Chalker, Two-dimensional random-bond Ising model, free fermions, and the network model, *Phys. Rev. B* **65**, 054425 (2002).
- [60] T. D. Schultz, D. C. Mattis, and E. H. Lieb, Two-Dimensional Ising Model as a Soluble Problem of Many Fermions, *Rev. Mod. Phys.* **36**, 856 (1964).
- [61] J. Hauschild and F. Pollmann, Efficient numerical simulations with Tensor Networks: Tensor Network Python (TeNPy), *SciPost Physics Lecture Notes* **5**, 5 (2018).
- [62] J. I. Cirac, D. Pérez-García, N. Schuch, and F. Verstraete, Matrix product states and projected entangled pair states: Concepts, symmetries, theorems, *Reviews of Modern Physics* **93**, 045003 (2021).

- [63] Y. Ma, M. Hanks, and M. S. Kim, Non–Pauli Errors Can Be Efficiently Sampled in Qudit Surface Codes, *Physical Review Letters* **131**, 200602 (2023).
- [64] V. Kolmogorov, Blossom V: a new implementation of a minimum cost perfect matching algorithm, *Mathematical Programming Computation* **1**, 43 (2009).
- [65] A. G. Fowler, A. C. Whiteside, and L. C. L. Hollenberg, Towards Practical Classical Processing for the Surface Code, *Physical Review Letters* **108**, 180501 (2012).
- [66] A. G. Fowler, Minimum weight perfect matching of fault-tolerant topological quantum error correction in average $O(1)$ parallel time, *Quantum Information and Computation* **15**, 145 (2015).
- [67] A. G. Fowler, M. Mariantoni, J. M. Martinis, and A. N. Cleland, Surface codes: Towards practical large-scale quantum computation, *Physical Review A* **86**, 032324 (2012).
- [68] S. Bravyi, M. Suchara, and A. Vargo, Efficient algorithms for maximum likelihood decoding in the surface code, *Physical Review A* **90**, 032326 (2014).
- [69] W. W. Ho, L. Cincio, H. Moradi, D. Gaiotto, and G. Vidal, Edge-entanglement spectrum correspondence in a nonchiral topological phase and Kramers-Wannier duality, *Physical Review B* **91**, 125119 (2015).
- [70] D. Aasen, R. S. K. Mong, and P. Fendley, Topological defects on the lattice: I. The Ising model, *J. Phys. A: Math. Theor.* **49**, 354001 (2016).
- [71] W. Ji and X.-G. Wen, Categorical symmetry and noninvertible anomaly in symmetry-breaking and topological phase transitions, *Physical Review Research* **2**, 033417 (2020).
- [72] T. Lichtman, R. Thorngren, N. H. Lindner, A. Stern, and E. Berg, Bulk anyons as edge symmetries: Boundary phase diagrams of topologically ordered states, *Physical Review B* **104**, 075141 (2021).
- [73] A. Chatterjee and X.-G. Wen, Symmetry as a shadow of topological order and a derivation of topological holographic principle, *Physical Review B* **107**, 155136 (2023).
- [74] D. S. Freed, G. W. Moore, and C. Teleman, Topological symmetry in quantum field theory, [arXiv:2209.07471](https://arxiv.org/abs/2209.07471).
- [75] H. Moradi, S. F. Moosavian, and A. Tiwari, Topological holography: Towards a unification of Landau and beyond-Landau physics, *SciPost Phys. Core* **6**, 066 (2023).
- [76] L. Bhardwaj and S. Schäfer-Nameki, Generalized Charges, Part II: Non-Invertible Symmetries and the Symmetry TFT, [arXiv:2305.17159](https://arxiv.org/abs/2305.17159).
- [77] L. Lootens, C. Delcamp, and F. Verstraete, Dualities in one-dimensional quantum lattice models: Topological sectors, *PRX Quantum* **5**, 010338 (2024).
- [78] L. Bhardwaj, L. E. Bottini, D. Pajer, and S. Schäfer-Nameki, Categorical Landau Paradigm for Gapped Phases, *Physical Review Letters* **133**, 161601 (2024).
- [79] V. Motamarri, C. McLauchlan, and B. Béri, SymTFT out of equilibrium: from time crystals to braided drives and Floquet codes, [arXiv:2312.17176](https://arxiv.org/abs/2312.17176).
- [80] H. Bombin and M. A. Martin-Delgado, Optimal resources for topological two-dimensional stabilizer codes: Comparative study, *Physical Review A* **76**, 012305 (2007).
- [81] D. Horsman, A. G. Fowler, S. Devitt, and R. V. Meter, Surface code quantum computing by lattice surgery, *New Journal of Physics* **14**, 123011 (2012).
- [82] Alternatively, one could consider the Bloch-sphere average [21, 22] of the infidelity between a generic logical state $|\psi_L\rangle$ and $X_L^q D_s [|\psi_L\rangle] X_L^q$, which yields $(2/3)P_{1-q,s}/P(s)$.
- [83] F. Eckstein, B. Han, S. Trebst, and G.-Y. Zhu, Robust Teleportation of a Surface Code and Cascade of Topological Quantum Phase Transitions, *PRX Quantum* **5**, 040313 (2024).
- [84] In the statistical-mechanics language, this equals the typical disorder correlator [85, 112, 113], i.e., the typical energy cost of flipping bonds along the logical X_L .
- [85] F. Merz and J. T. Chalker, Negative scaling dimensions and conformal invariance at the Nishimori point in the $\pm J$ random-bond Ising model, *Physical Review B* **66**, 054413 (2002).
- [86] A. S. Darmawan, Optimal adaptation of surface-code decoders to local noise, [arXiv:2403.08706](https://arxiv.org/abs/2403.08706).
- [87] Z. Cheng, E. Huang, V. Khemani, M. J. Gullans, and M. Ippoliti, Emergent unitary designs for encoded qubits from coherent errors and syndrome measurements, [arXiv:2412.04414](https://arxiv.org/abs/2412.04414).
- [88] M. J. Gullans and D. A. Huse, Dynamical Purification Phase Transition Induced by Quantum Measurements, *Physical Review X* **10**, 041020 (2020).
- [89] O. Higgott, Pymatching: A python package for decoding quantum codes with minimum-weight perfect matching, [arXiv:2105.13082](https://arxiv.org/abs/2105.13082).
- [90] O. Higgott and C. Gidney, Pymatching v2, <https://github.com/oscarhiggott/PyMatching> (2022).
- [91] M. Baranger, Problem of Overlapping Lines in the Theory of Pressure Broadening, *Phys. Rev.* **111**, 494 (1958).
- [92] I. Bengtsson and K. Życzkowski, *Geometry of Quantum States: An Introduction to Quantum Entanglement* (Cambridge University Press, Cambridge, U.K., 2006).
- [93] A. Gilchrist, D. R. Terno, and C. J. Wood, Vectorization of quantum operations and its use, [arXiv:0911.2539](https://arxiv.org/abs/0911.2539).
- [94] F. A. Bais and J. K. Slingerland, Condensate-induced transitions between topologically ordered phases, *Physical Review B* **79**, 045316 (2009).
- [95] L. Kong, Anyon condensation and tensor categories, *Nuclear Physics B* **886**, 436 (2014).
- [96] F. Burnell, Anyon Condensation and Its Applications, *Annual Review of Condensed Matter Physics* **9**, 307 (2018).
- [97] M. S. Kesselring, J. C. Magdalena de la Fuente, F. Thomsen, J. Eisert, S. D. Bartlett, and B. J. Brown, Anyon Condensation and the Color Code, *PRX Quantum* **5**, 010342 (2024).
- [98] C. Nayak, S. H. Simon, A. Stern, M. Freedman, and S. Das Sarma, Non-Abelian anyons and topological quantum computation, *Reviews of Modern Physics* **80**, 1083 (2008).
- [99] X. G. Wen and A. Zee, Classification of Abelian quantum Hall states and matrix formulation of topological fluids, *Physical Review B* **46**, 2290 (1992).
- [100] X.-G. Wen, Topological orders and edge excitations in fractional quantum hall states, *Advances in Physics* **44**, 405 (1995).
- [101] F. D. M. Haldane, Stability of Chiral Luttinger Liquids and Abelian Quantum Hall States, *Physical Review Letters* **74**, 2090 (1995).
- [102] X.-G. Wen, *Quantum Field Theory of Many-Body Systems: From the Origin of Sound to an Origin of Light*

- and Electrons* (Oxford University Press, Oxford, U.K., 2007).
- [103] T. Giamarchi, *Quantum Physics in One Dimension* (Oxford University Press, Oxford, U.K., 2003).
- [104] A. Biella and M. Schiró, Many-Body Quantum Zeno Effect and Measurement-Induced Subradiance Transition, *Quantum* **5**, 528 (2021).
- [105] X. Turkeshi, A. Biella, R. Fazio, M. Dalmonte, and M. Schiró, Measurement-induced entanglement transitions in the quantum Ising chain: From infinite to zero clicks, *Physical Review B* **103**, 224210 (2021).
- [106] S. W. Yan, D. Barberena, M. P. A. Fisher, and S. Vijay, Dissipative Dynamical Phase Transition as a Complex Ising Model, [arXiv:2412.09591](https://arxiv.org/abs/2412.09591).
- [107] A. Luther and V. J. Emery, Backward Scattering in the One-Dimensional Electron Gas, *Physical Review Letters* **33**, 589 (1974).
- [108] G.-Y. Zhu, N. Tantivasadakarn, A. Vishwanath, S. Trebst, and R. Verresen, Nishimori's Cat: Stable Long-Range Entanglement from Finite-Depth Unitaries and Weak Measurements, *Physical Review Letters* **131**, 200201 (2023).
- [109] X. Turkeshi and P. Sierant, Error-resilience Phase Transitions in Encoding-Decoding Quantum Circuits, [arXiv:2308.06321](https://arxiv.org/abs/2308.06321).
- [110] S. Anand, M. Zaletel, and Y. Bao, Efficient algorithms for sampling and maximum-likelihood decoding in the surface code with local noise (2025), in preparation.
- [111] The total number of parameters reduces to 12 when taking into account that $\mathcal{E}_j^{(f)}$ is traceless [9].
- [112] L. P. Kadanoff and H. Ceva, Determination of an Operator Algebra for the Two-Dimensional Ising Model, *Physical Review B* **3**, 3918 (1971).
- [113] N. Read and A. W. W. Ludwig, Absence of a metallic phase in random-bond Ising models in two dimensions: Applications to disordered superconductors and paired quantum Hall states, *Physical Review B* **63**, 024404 (2000).